Iron mineral dissolution releases iron and associated organic carbon during permafrost thaw

Monique S. Patzner[1], Carsten W. Mueller[2,3], Miroslava Malusova[1], Moritz Baur[1], Verena Nikeleit[1], Thomas Scholten[4], Carmen Hoeschen[2], James M. Byrne[1,6], Thomas Borch[5], Andreas Kappler[1] & Casey Bryce[1,6]*

[1] Geomicrobiology, Center for Applied Geosciences, University of Tuebingen, Tuebingen, Germany.

[2] Chair of Soil Science, Technical University Muenchen, Freising, Germany.

[3] Department of Geosciences and Natural Resource Management, University of Copenhagen, Denmark.

[4] Chair of Soil Science and Geomorphology, University of Tuebingen, Germany.

[5] Department of Soil & Crop Sciences and Department of Chemistry, Colorado State University, Fort Collins, US.

[6] School of Earth Sciences, University of Bristol, Bristol, UK.

*Corresponding Author: Casey Bryce

School of Earth Science, Wills Memorial Building, University of Bristol, Queens Road, Bristol, BS8 1RJ

Email: casey.bryce@bristol.ac.uk

Keywords: Soil organic carbon, iron carbon associations, iron reduction, selective extractions, nanoSIMS, EXAFS, Abisko, Arctic, peatland

Brief/running title: Mineral dissolution during permafrost thaw

Abstract

It has been shown that reactive soil minerals, specifically iron(III) (oxyhydr)oxides, can trap organic carbon in soils overlying intact permafrost, and may limit carbon mobilization and degradation as it is observed in other environments. However, the use of iron(III)-bearing minerals as terminal electron acceptors in permafrost environments and thus their stability and capacity to prevent carbon mobilization during permafrost thaw is poorly understood. We have followed the dynamic interactions between iron and carbon, using a "space for time" approach, across a thaw gradient in Abisko (Sweden), where wetlands are expanding rapidly due to permafrost thaw. We show through bulk (selective extractions, EXAFS) and nanoscale analysis (correlative SEM and nanoSIMS) that organic carbon is bound to reactive Fe primarily in the transition between organic and mineral horizons in palsa underlain by intact permafrost. During thaw, water-logging and O_2 limitation lead to reducing conditions and an increase in abundance of Fe(III)-reducing bacteria which favor mineral dissolution and drive mobilization of both iron and carbon along the thaw gradient. By providing a terminal electron acceptor, the "rusty carbon sink" is effectively destroyed along the thaw gradient and cannot prevent carbon release with thaw.

Main Text

Introduction

The release of vast amounts of organic carbon during thawing of high-latitude permafrost is an emerging issue of global concern. Yet it is unclear, if mineral stabilization can control the amount of this released carbon that will be subsequently metabolized and emitted as greenhouse gases. Reactive iron minerals (defined here as iron minerals that are reductively dissolved by the chemical reductant sodium dithionite, e.g. ferrihydrite or goethite) are known to stabilize organic carbon by sorption and co-precipitation[1] and are thought to significantly influence long-term carbon storage in numerous environments[2-5]. The inventory of reactive iron minerals in natural systems is highly dynamic as they precipitate and dissolve in response to changing redox conditions. When mineral dissolution occurs, iron and carbon mobilization, increased carbon lability/bioavailability, and increased gaseous carbon loss as CO_2 and CH_4 could follow (catalyzed by heterotrophic and methanogenic microorganisms)[6-10]. Despite the importance of iron minerals for carbon storage, we have little understanding of the presence of this "rusty carbon sink" in organic-rich permafrost peatlands and even less knowledge of how it will respond to changing redox conditions associated with permafrost thaw.

In order to address this knowledge gap, we examined peatland soils collected along a thaw gradient at Stordalen mire (Abisko, Sweden). For this study, three thaw stages were defined based on shifts in vegetation and hydrology, as has been done previously[11-14], and known changes in microbial ecology[15,16] (Fig. 1, Fig. S5). These are: (1) desiccating palsa underlain by permafrost, (2) intermediately thawed bog, and (3) fully-thawed fen. Desiccating palsa sites are mainly dry and oxic[12]. As the permafrost thaws, the raised, dry ombrotophic palsas collapse, causing enlargement of semiwet and wet ombrotrophic bog areas with continuously frozen soil underneath[12,13]. With continued thawing, the bog areas decrease and minerotrophic fen areas expand with complete water saturation and thus even more reducing conditions than in the

bog[11-13]. To be able to use a "space for time" approach, the habitats are ordered following a temporal succession of apparent time since onset of thaw, as has been done by Hodgkins *et al*[12].

We collected cores from locations deemed most representative of the three thaw stages and analyzed iron-carbon associations in three different layers within the cores defined by geochemical stratification, as done previously[17]. Cores were split into (1) organic horizon, (2) transition zone, interface between the two soil horizons, which can be locally very sharply defined (3-5 cm), but also reach over 20 cm depth[17], and (3) mineral horizon. We analyzed the solid phase by selective extractions to determine different iron phases such as reactive iron (dithionite citrate extractable), poorly crystalline iron (hydroxylamine HCl), colloidal and OM-chelated iron (sodium pyrophosphate), and crystalline iron phases (6M HCl). The selective extractions were simultaneously used to determine iron-bound carbon by measurement of DOC in the sodium dithionite citrate and sodium pyrophosphate extractions. Extended X-ray absorption fine structure (EXAFS) analysis was performed to support extraction data and further determine the presence of phases such as Fe-containing clays which were not extracted by the selective dissolutions. Correlative scanning electron microscopy (SEM) and nanoscale secondary ion mass spectrometry (nanoSIMS) were used to visualize iron-carbon associations in the fine fraction of the different soil layers. This was complemented by geochemical analysis of the porewater to determine potential electron acceptors and donors, and to track iron and carbon release from the solid into the liquid phase. Additionally, Fe(III)-reducing bacteria which are the driving force behind iron mineral reduction under anoxic conditions were quantified by a growth-dependent approach.

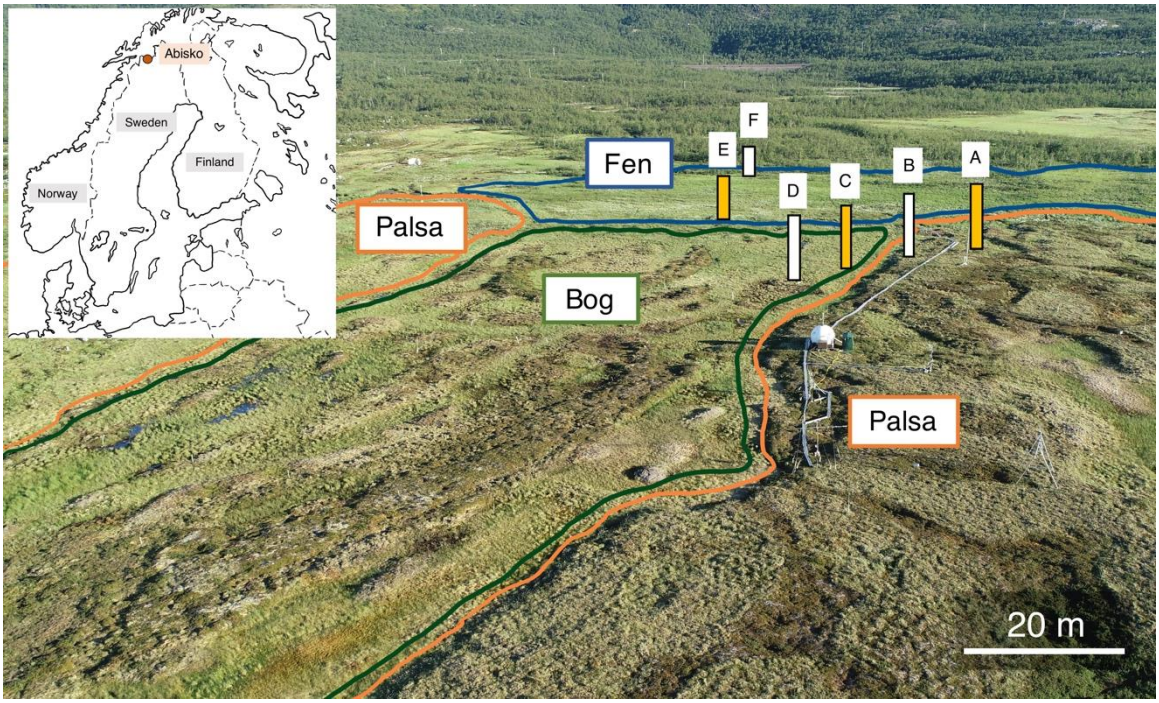

Fig. 1. Field site Stordalen mire close to Abisko in the north of Sweden. The three main thaw stages are (1) palsa (marked in orange), (2) bog (in green) and (3) fen (in blue). The positions of the three cores analyzed in detail within 3-4 days of collection, which represent all three thaw stages, are shown in yellow. Additional cores (shown in white) were taken and analyzed after 7 months of incubation at 4°C (S5, Fig. S5 and Fig. S6). Data for further replicates is provided in the SI (S5, Figs. S7-S8).

Thaw increases aqueous Fe^{2+} and dissolved organic carbon

Along the thaw gradient, the aqueous Fe^{2+} in the porewater increased from average concentrations of 0.02±0.01 mM in the palsa to up to 1.6±0.3 mM in the fen transition zone (Fig. 2). This correlates with an increase in average dissolved organic carbon (DOC) from 19.7±0.8 mg/L in the palsa to 102.1±14.1 mg/L in the fen area. In the bog porewater, acetate (0.6±0.1 mM) was measurable in the mineral horizon, whereas lactate (0.8±0.02 mM) was only found in the transition zone. (Fig. 2). At the fen site, lactate and acetate were detected throughout the depth profile (0.2±0.1 mM). An additional peak in acetate (2.3±0.01 mM), propionate (0.8±0.02 mM) and butyrate (0.2±0.01 mM) was observed in the transition zone of the fen (Fig. 2). The appearance of butyrate and propionate in the fen porewater could be an

indicator for ongoing microbial processes such as fermentation and methanogenesis in the more water-logged and thus more reduced fen soils. This is in line with observations from previous studies that show highest methane emissions occur in the fen[15]. Our porewater data along the thaw gradient clearly shows an increase in aqueous Fe^{2+} and more labile organic carbon. It also highlights unique biogeochemical processes in the transition zone leading to the consumption or accumulation of fatty acids in this layer. The presence of more labile organic carbon in the porewater is consistent with previous work[12].

The abundance of Fe(III)-reducing bacteria increases with thaw

The trend in increasing aqueous Fe^{2+} and DOC concentrations observed across the thaw gradient goes hand in hand with a significant increase in abundance of Fe(III)-reducing bacteria in the organic horizon from palsa to fen (unpaired t-test, n=7, α=0.05, p=0.0001), and a significant increase in the transition zone from palsa to fen (unpaired t-test, n=7, α=0.05, p=0.0001). In the mineral horizon at all three thaw stages, no difference in abundance of Fe(III)-reducing cells was observed ($2x10^3$ cells per g soil). In the palsa organic horizon, $2.4x10^2$ cells per g soil were found, in comparison to $2.6x10^4$ cells per g soil in the organic horizon in the fen. In the transition zone of palsa, $2.4x10^3$ cells per g soil were determined. Whereas, in the fen transition zone the highest abundance of Fe(III)-reducing bacteria was $3.1x10^5$ cells per g soil. The abundance of Fe(III)-reducing bacteria was determined via growth by the Most Probable Number method (MPNs). Further isolation efforts from the fen yielded a microorganism with 99% similarity on the 16S rRNA level to *Cupriavidus metallidurans* (Proteobacteria). The isolate was able to reduce ferrihydrite to Fe(II) whilst simultaneously consuming lactate and producing acetate via anaerobic fermentation (Fig. S10). It did not utilize acetate. *Cupravidus metallidurans* strains are known to be extremely metabolically flexible and can utilize lactate under anoxic conditions[18]. They are also highly tolerant of toxic metals[18].

Although Fe(III) reduction is usually thought of as a dissimilatory process, in some peatlands, Fe(III) reduction coupled to fermentative metabolisms have been observed to be more common[19]. This could be one explanation for the acetate peak in the fen transition zone and increasing Fe(II) concentrations in the fen. Woodcroft *et al* (2018)[16] describes evidence of fermentation along this thaw gradient and found Proteobacteria as one of the primary lactate metabolizers in the fen. Our growth-dependent quantification is suggestive of increased microbially-driven Fe(III) mineral dissolution along the thaw gradient (Fig. 2).

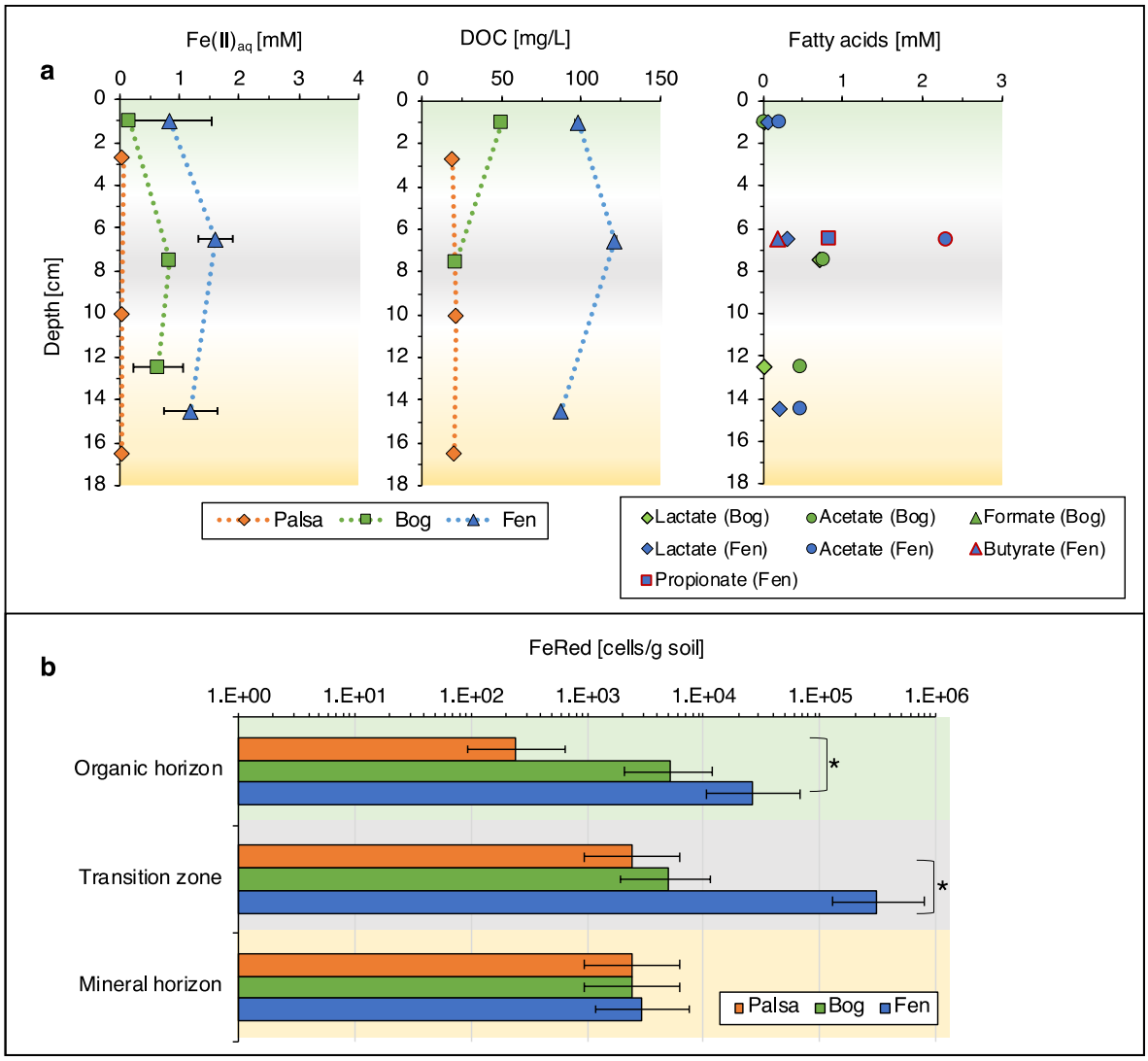

Fig. 2. a, Porewater geochemical analysis of the cores Palsa A, Bog C and Fen E and b, most probable number quantifications of Fe(III)-reducing bacteria (FeRed) in the solid phase of the cores Palsa A, Bog C and Fen E along the thaw gradient. Red outline marks the high acetate concentrations in the fen, in comparison to the bog, and the

additional fatty acids butyrate and propionate, only detected in the fen. The error bars of the porewater data represent triplicate measurements. The error bars of the most probable number estimations of Fe(III)-reducers represent 7 replicate analyses and indicate lower and upper limits of the 95% confidence intervals. * marks significant difference between FeRed in palsa and fen, organic horizon and transition zone (unpaired t-test, n=7, α=0.05, p=0.0001). The green background marks the organic horizon, grey the transition zone, and yellow the mineral horizon. The backgrounds for the porewater geochemistry are shaded due to the fact that this represents three cores, one core per thaw stage, with different horizon depths.

Reactive iron minerals are dissolved along the thaw gradient

In order to determine whether the observed increases in DOC were related to increased Fe(III) mineral reduction and dissolution, we quantified the amount of organic carbon associated with the reactive iron minerals along the thaw gradient by applying the citrate-dithionite iron reduction method[4,20,21]. This method simultaneously dissolves all reactive solid iron phases and releases the organic carbon associated with these minerals into solution. The extraction is performed at circumneutral pH to prevent hydrolysis of organic matter as well as its protonation and re-adsorption onto the remaining solid phases and thus its precipitation. A control experiment was conducted at the same pH with equivalent ionic strength (sodium chloride instead of the reducing agent sodium dithionite). The organic carbon which is released in this control is not associated with the reactive iron minerals and was therefore subtracted from the amount of carbon released from the dithionite-citrate extraction as previously described[4] (Table S1). Well-known issues with these extractions and a discussion of how we have overcome these are included in the Supplementary Information (S2, S3). Additionally, we performed a sodium hydroxylamine-HCl extraction (pH<2) to target the poorly crystalline iron minerals, a sodium pyrophosphate extraction (pH 10) to extract colloidal or OM-chelated iron, and a 6M HCl extraction to obtain more crystalline iron phases of the soil layers (referred to as mg Fe(tot) per g) (Fig. 3). It should be noted that the total amount of iron per dry weight in the

layers is different along the thaw gradient due to different redox-driven biogeochemical cycles in the three different thaw stages resulting in loss of total soil organic carbon and thus in an increasing abundance of the mineral material present in the active layer (Fig. S6 and Fig. S7 for spatial and horizontal variance in replicate cores). In the following, only the data from cores Palsa A, Bog C and Fen E are discussed (Fig. 1, Fig. 3 and Fig. 4), but observed trends are supported by further analyses conducted on cores collected at the same time but stored for a longer period (Palsa B, Bog D, Fen F) (S5), and on triplicate cores from each thaw stage (S5). In the transition zone of the palsa, the reducible iron mineral fraction was 72.9 to 93.9% of the total extractable iron (2.6±0.6 to 8.4±0.2 mg reactive Fe per g soil in comparison to 3.5±0.1 to 9.0±0.3 mg Fe(tot) per g soil) (Fig. 3, Table S1, S5). The amount of reactive iron minerals in the transition zone then decreased to 11.1% of the total extractable iron in the bog (2.1±0.1 mg reactive Fe per g soil in comparison to 18.7±0.7 mg Fe(tot) per g soil) and to 18.3% of the extractable iron in the fen (2.6±0.03 mg reactive Fe per g soil in comparison to 14.5±0.2 mg Fe(tot) per g soil) (Fig. 3, Table S1, S5). In the mineral horizons along the thaw gradient, a loss of the reactive iron minerals was also observed, likely due to more reduced conditions favoring Fe(III) mineral reduction at deeper depths. Reactive iron in the palsa mineral layer was 10.0 to 36.6% of the total extractable iron (3.2±0.2 to 1.4±0.2 mg reactive Fe per g soil in comparison to 8.7±0.3 to 13.5±0.2 mg Fe(tot) per g soil) and declined to 7.5% of the total extractable iron in the bog (0.9±0.1 mg reactive Fe per g soil in comparison to 11.7±0.8 mg Fe(tot) per g soil) and 9.0 to 10.7% of the total iron in the fen (1.8±0.04 to 1.7±0.04 mg reactive Fe per g soil in comparison to 16.3±0.4 to 19.01±0.25 mg Fe(tot) per g soil) (Fig. 3, Table S1, S5). This loss of reactive iron in the transition zone and mineral horizon was also confirmed by the hydroxylamine-HCl extraction and iron speciation by EXAFS (Fig. 3). The abundance of colloidal and/or OM-complexed iron (defined as sodium pyrophosphate extractable iron) also decreased along the thaw gradient, giving way to an increasing relative atom percent-based

abundance of Fe-bearing clays (Fig. 3). This observation is consistent with increasing aluminum concentrations in the extracts (Fig. S4). The iron content in the organic layer increased from almost no iron in the palsa (0.2±0.02 mg Fe(tot) per g soil, all poorly crystalline) to 4.7±0.01 mg Fe(tot) per g soil (with 43.4% of the total extractable iron being reactive iron) in the organic layer of the fen (Fig. 3, S5). We suggest this is driven by Fe(III) reduction in deeper layers leading to mobilization of Fe(II), which might precipitate again close to the water surface by oxidation of Fe(II) by O_2, which diffuses from the surface, followed by precipitation as Fe(III) oxyhydroxide minerals, as has been also previously suggested for boreal peat soils[22].

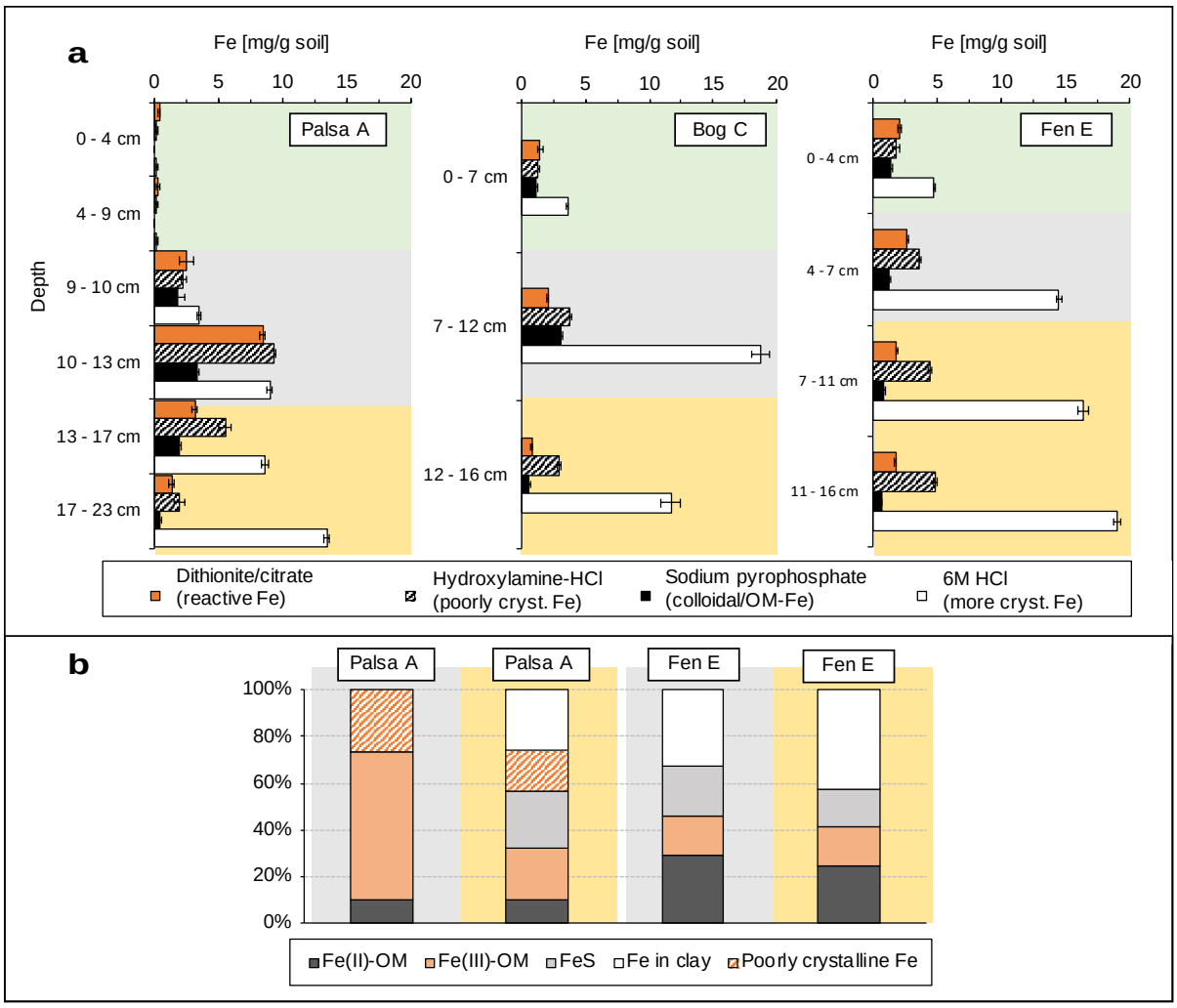

Fig. 3. Fe speciation along the thaw gradient determined by a, selective extractions and b, EXAFS. The reactive iron mineral fraction [mg Fe per g soil] was quantified in the different layers and compared to the more crystalline Fe (6M HCl extractable Fe, referred to mg Fe(tot) per g soil in the text) and to the colloidal and/or OM-chelated

Fe (sodium pyrophosphate). Please note the differences in the scale of y-axis due to variable thickness of each soil layer along the thaw gradient. The green background marks the organic horizon, grey the transition zone, and yellow the mineral horizon. Error bars represent duplicate extractions of each layer per thaw stage. EXAFS results of the transition zone and the mineral horizon of the two-end members palsa and fen show loss of the poorly crystalline Fe (reference probe: 2-line ferrihydrite), the decrease in OM-chelated Fe (reference probes: Fe(II)-citrate and Fe(III)-citrate), the increase of Fe in clays (reference probes: natural nontronite and ferrosmectite) and Fe sulfur species (reference probe: mackinawite) with depth and along the thaw gradient. Absolute values are reported in Table S1 (also see S2-S5).

Dissolution of reactive iron minerals releases associated organic carbon

With the dissolution of reactive iron minerals along the thaw gradient, the mineral-associated carbon was mobilized. Organic carbon bound to the reactive iron phases is primarily found in the transition zone and the mineral horizon of the palsa, as well as in the transition zone of the bog (Fig. 4, S1 Table S1, S5). 9.9 to 14.8% of the total organic carbon (31.0±0.7 to 52.5±0.1 mg organic carbon bound to reactive Fe per g soil in comparison to 312.1±0.3 to 354.7±0.04 mg total soil organic carbon per g soil) was released by reductive dissolution of reactive iron minerals in the palsa transition (Fig. 4, Table S1, S5). In the palsa mineral horizon, 18.7 to 20.1% of the total organic carbon (13.6±0.4 to 27.4±1.6 mg organic carbon bound to reactive Fe per g soil in comparison to 72.7±0.29 to 136.1±0.2 mg total soil organic carbon per g soil) was released. In the transition zone of the bog, 39.4% of the total organic carbon (22.7±8.6 mg organic carbon bound to reactive Fe per g soil in comparison to 57.5±0.4 mg total soil organic carbon per g soil) was associated with iron minerals (Fig. 4, Table S1, S5). However, it should be noted that the total amount of carbon was less in the bog transition zone (57.5±0.4 mg total soil organic carbon per g soil) when compared to the palsa transition zone (312.1±0.3 to 354.7±0.04 mg total soil organic carbon per g soil) due to total carbon loss along the thaw gradient. Highest total amounts of carbon bound by the reactive iron were therefore

found in the palsa transition zone with an average of 41.8±10.8 mg per g soil. This is also supported by the strong spatial association of C with Fe minerals in the fine fraction of this transition zone observed by nanoSIMS analysis (Fig. 4, Fig. S9), as has been also previously shown for intact permafrost soils[23]. The maximum molar ratio of organic carbon to iron of 1.0, based on the maximal sorption capacity of reactive iron oxides for natural organic matter[24], as has been previously done to further characterize Fe-C associations in such systems[25,26], was exceeded in the bulk palsa transition zone and bulk palsa mineral horizon (9.27±2.16 OC:Fe). This suggests co-precipitation and/or chelation of organic compounds also in the bulk sample which can generate structures with OC:Fe ratios of 6 to 10, as shown in other studies[24], and are consistent with high sodium pyrophosphate extractable iron values and the fine fraction analysis for these palsa layers.

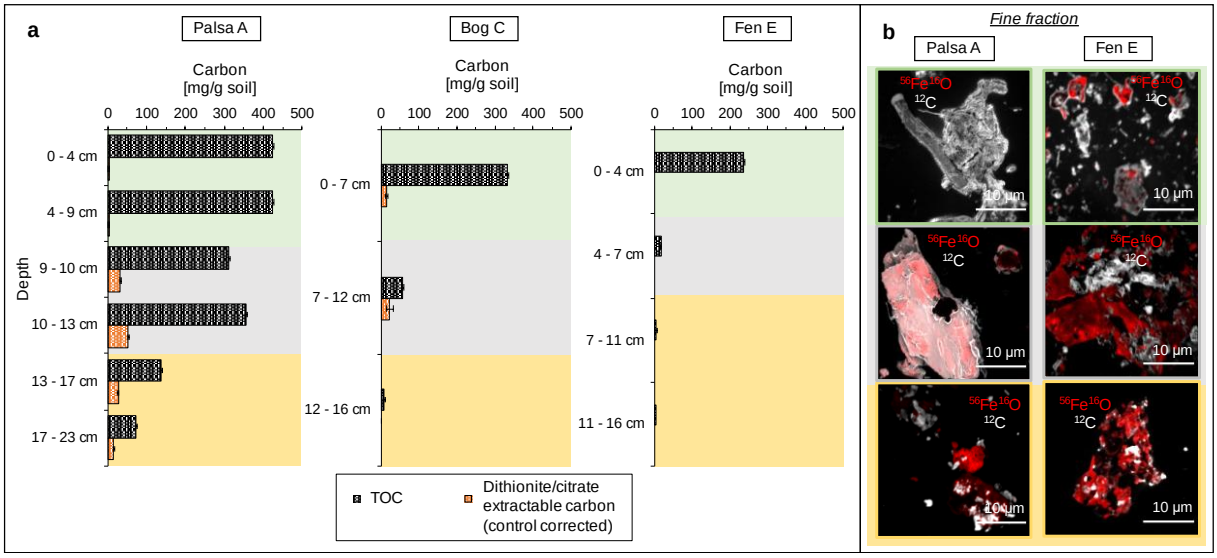

Fig. 4. Fe-C associations along the thaw gradient determined by a, bulk and b, fine fraction analysis. a, Carbon bound by reactive iron minerals along the thaw gradient. The carbon which dislodged from the soil during the reductive dissolution of reactive iron oxides (orange) is shown in comparison to the total organic carbon determined via combustion (black grids, labeled as TOC). Dithionite-citrate extractable carbon is "control corrected" by subtracting the measured DOC content of a citrate solution and the measured DOC value from the NaCl control experiment. The NaCl control (same ionic strength and same pH as the sodium dithionite citrate extraction) shows negligible carbon release (Table S1, S2-S5). Errors indicate the range of duplicate analyses of

each layer in each thaw stage. b, High spatial resolution analysis of iron-carbon associations by nanoSIMS along the thaw gradient (two end-members palsa (left) and fen (right)). The strong spatial association of C to Fe(III) minerals could only be observed in the palsa transition zone. The other fine fractions showed organic-free iron minerals. For the two end-members palsa and fen, four particles of the fine fractions of each layer were analyzed by nanoSIMS, all showing the same spatial distribution of Fe and C as shown by these six representatives (see also Fig. S9). The green background marks the organic horizon, grey the transition zone, and yellow the mineral horizon.

Implications for stability of Fe-associated carbon

Carbon binding to reactive iron minerals in the palsa area is consistent with previous observations in permafrost regions of the Qinghai-Tibet Plateau[21] where Fe associated organic carbon represents, on average, 19.5±12.3% of the total soil organic carbon pool in the upper 30 cm of permafrost soils throughout the year. Assuming a carbon pool of 191.29 x 10^{15} g carbon in the active layer (0-30 cm depth)[27] in northern permafrost regions, we suggest that 13.39 x 10^{15} to 38.26 x 10^{15} g carbon could potentially be bound to reactive iron in permafrost soils. The lower estimate assumes, based on our data, an average of 7% of total organic carbon is bound to reactive iron in active layers underlain by intact permafrost (Table S1, average mg C bound to reactive Fe per g soil in comparison to average mg TOC per g soil in %). The higher estimate assumes a maximum of 20% of total organic carbon is bound to reactive iron, based on our data (Table S1) and Mu *et al* (2016)[21]. This Fe-bound carbon stock is equivalent to approximately 2 to 5% of the amount of carbon which is currently present in the atmosphere. Although this estimate does not account for deeper layers. With progressive climate change active layers will deepen and even higher amounts of carbon could be bound to reactive Fe. It is therefore crucial to further determine the amount of carbon bound to reactive iron minerals in numerous permafrost environments, and the lability/bioavailability of this carbon following its release.

Our "space for time" approach reveals, for the first time, how we may expect the dynamics of this rusty carbon sink to respond to progressive climate change. This study suggests that, as soon as the conditions in permafrost peatlands become water-logged, the reactive iron minerals are reduced, probably by Fe(III)-reducing bacteria, and dissolved iron and associated organic carbon are released into the surrounding porewater. Since Fe(III) reduction is more thermodynamically favorable, conditions more suitable for Fe(III)-reducers can inhibit methanogenesis[28]. However, Fe(III) reduction consumes protons and help increase pH which can make conditions more favorable for methanogens[29]. Along the thaw gradient, an increase in pH and an increasing abundance of methanogens has been reported[15]. Acetotrophic methanogens can use Fe(III) reduction to maximize energy conservation from metabolism of acetate[30]. Shifts in CH_4 production pathway from CO_2 to acetate cleavage along the thaw gradient was previously described[12,15]. At the same time, anaerobic oxidation of methane by methanotrophs can also be coupled to Fe(III) reduction. An increase in methane oxidation rates along the thaw gradient has been shown by Perryman *et al* (2020)[31]. Our data clearly shows that reactive Fe phases serve as an important and overlooked terminal electron acceptor along the thaw gradient and thus could exert a significant control on net methane emissions.

Furthermore, the released aqueous Fe^{2+} could be complexed by organic carbon[5] along the thaw gradient, inhibiting re-oxidation even when oxygen concentrations are high. The peatland at Stordalen mire could be a significant source of bioavailable iron to surrounding lakes and rivers, as has been shown at other permafrost environments[32]. It has also been shown that Fe(III) minerals can act as "sieves" for DOM by selectively trapping terrestrially derived OM (enriched in aromatic moieties) on mineral surfaces at redox interfaces[5]. More work is needed to elucidate the chemical nature of associated organic carbon to determine its lability, but our data suggest that direct chelation or co-precipitation of Fe-C structures play an essential role in carbon protection.

In order to better predict future greenhouse gas emissions from thawing permafrost soils and improve the accuracy of existing climate models, it is therefore crucial to further determine Fe(III) reduction rates, its direct contribution to CO_2 emissions from peatland mires and its competition with other microbial processes, such as e.g. methanogenesis or methanotrophy.

Materials and Methods

Site description and sample collection

Stordalen mire is a peatland 10 km southeast of Abisko in northern Sweden (68 22′ N, 19 03′ E)[33] which is underlain by quartz-feldspar-rich sedimentary rock (Geological Survey of Sweden). The study site is within the discontinuous permafrost region of northern Scandinavia and consists of three distinct sub-habitats which are common to northern wetlands: (1) a well-drained palsa underlain by permafrost, dominated by ericaceous and woody plants, (2) a bog with variable water table depth and some active thawing, dominated by *Sphagnum* spp. mosses, and (3) a fully-thawed and inundated fen, dominated by sedges such as *Eriophorum angustifolium*[12,13]. In this study, the three sub-habitats were ordered following a temporal succession of apparent time from "palsa", to "bog" and "fen", a "space for time" approach, as has been done before[12] following the classification of Johansson *et al* (2006)[13]. This approach is limited in that (1) permafrost thaw progression through these three thaw stages is not necessarily linear[12], (2) intermediate thaw stages (e.g. collapsed palsa) are not accounted for, and (3) it does not fully capture the heterogeneity of the landscape. However, this approach provides the best available estimate of how palsa mires will evolve with progressive climate change and thus has been applied widely at this site. The palsa and bog areas are underlain by permafrost with a thickness of 10-20 m[34]. The active layer, depending on the surface topography, ranges from 0.5-1 m thickness at maximum thaw[34,35]. These three thaw stages cover ~98% of the mire's non-lake surface[12]. A thaw-dependent shift in these habitats was

observed from 1970 to 2000 during which palsa regions collapsed and bog and fen areas increased by 17%[11]. At the same time, an increase in average annual temperature by 2.5°C between 1913 and 2006 was measured, resulting in an annual mean temperature >0°C during the recent decades[36]. The total precipitation also increased during this period of time to an annual average of 306 mm (NORDKLIM, data available at http://www.smhi.se/hfa_coord/nordklim). The expansion of wetlands after permafrost melt is a widespread characteristic of peatlands affected by permafrost thawing[37-40] and the successional shift from palsa to bog and fen areas has been documented in other northern peatlands[39-42].

In July 2018, cores were taken in duplicates along a gently collapsing thaw gradient from palsa to bog and fen (Fig. S5). Stordalen mire is a protected area with other ongoing field research, thus the extent of coring is strictly limited due to the risk of accelerating permafrost thaw and/or disturbance to other long-term measurements, especially at sensitive sites like erosion fronts. However, extensive context data (https://polar.se/en/research-in-abisko/research-data/) from the Abisko scientific community is available which ensures representative field sampling of a heterogeneous permafrost area, with cores taken following a transect along the direction of hydrological flow from palsa to bog and fen as described by Olefeldt and Roulet (2012)[43]. Given the restrictions in place, it was only possible to collect five cores per each thaw stage (S5) over to field campaigns (2017 and 2018). A Humax corer of 50 cm length and 3-cm-diameter with inner core liners was used. The inner liners were washed three times with 80% ethanol, six times with sterile MilliQ water and sealed with sterilized butyl rubber stoppers until coring. Butyl rubber stoppers were boiled three times in deionized water and sterilized at 121°C for 20 min in an autoclave. Sharp edges were cut into the end of the coring device to help cut the peat layer. A hammer was used to further sample the active layer. Hammering caused compaction of the cores. Therefore, the recorded depths are not comparable to the initial soil profiles and the data is presented by different layers rather than

depth. In the palsa and bog area, cores were taken until the depth of the ground ice. Layers at the bottom of the core which contained predominantly ice were excluded from further analyses. Therefore, the soil investigated in this study represented the seasonally thawed active layer at Stordalen mire, ranging from 30 to 49 cm. The cores were stored vertically at 4°C in the dark. Three cores representing desiccating palsa, bog and fen were processed within 3-4 days (Fig. S5). Due to detailed analysis of the first core set (Palsa A, Bog C and Fen E), additional cores (Palsa B, Bog D and Fen F) from each thaw stage were analyzed after storage for 7 months at 4°C in the dark, which is not ideal, but still could be used to determine if preservation of the carbon by reactive iron was stable over longer time periods (Fig. S5 and Fig. S6). The long-term stored core Palsa B still showed higher abundance of reactive iron minerals than Bog D and Fen F, but less than Palsa A which could be due to natural variability, long-term storage or because it was taken closer to the collapsing edge (Fig. S5 and Fig. S6). The cores A to F were compared to triplicate cores previously collected in September 2017 at each thaw stage with a Pürckhauer corer and processed directly after sampling, to show that the trends are representative for the whole mire (Fig. S5, Fig. S7 and Fig. S8). The replicate cores showed the same trends of 6 M HCl extractable iron. Readily extractable Fe (defined by 0.5 M HCl extractable iron) showed similar trends to the sodium dithionite citrate or hydroxylamine HCl extraction for all three thaw stages (Fig. S7). The same trend of total organic carbon along the thaw gradient was observed (Fig. S8).

Porewater sampling and analysis

The cores were kept in a vertical position during transfer into an anoxic glovebox (100% N_2). Three different sections were identified by texture and color changes: (1) an organic horizon on top, (2) a middle transition zone between the organic-rich and mineral-rich layer and (3) a mineral horizon at the bottom (Fig. S5). Rhizon porewater samplers (Rhizosphere research products, Netherlands) with a porous sampling area of 10 cm and 0.15 µm pore size

were used to extract porewater from three different depths, resulting in one sample representing each organic horizon, transition zone and mineral horizon. The extracted porewater was analyzed for dissolved Fe (total and Fe(II)), organic carbon (DOC) and fatty acids. The samples were centrifuged for 5 min at 5300 g. For total Fe and Fe(II), the supernatant was acidified in 1 M hydrochloric acid (HCl) and quantified spectrophotometrically in triplicate with the ferrozine assay[44]. Dissolved OC was quantified in triplicate with a total organic carbon analyzer (High TOC II, Elementar, Elementar Analysensysteme GmbH, Germany). High performance liquid chromatography (HPLC; class VP with refractive index detector [RID] 10A and photo-diode array detector SPD-M10A VP detectors; Shimadzu, Japan) was used to determine the fatty acid concentrations.

Core splitting

The soil cores were removed from their liners under N_2 atmosphere. Each core was sectioned into an organic horizon of varying thickness (4-10 cm), a transition zone (3-5 cm) and mineral horizon (4-10 cm) (Fig. S5), following Ryden *et al* (1980)[17]. The transition zone represents the boundary between organic and mineral horizon and was additionally defined due to distinct geochemical conditions in the porewater analysis in the middle of the active layer near the boundary between organic and mineral horizon. Calculated bulk densities as a function of soil organic matter following Bockheim *et al* (2003)[45] were consistent with other studies conducted at Stordalen mire[17] (Palsa A: organic horizon: 0.03±0.01 g/cm^3, transition zone: 0.08±0.02 g/cm^3, mineral horizon: 0.84±0.26 g/cm^3; Bog C: organic horizon 0.08±0.01 g/cm^3, transition zone 1.29±0.04 g/cm^3 and mineral horizon 1.74±0.01 g/cm^3, Fen E: organic horizon 0.21±0.02 g/cm^3, transition zone 1.97±0.2 g/cm^3 and mineral horizon 1.72±0.01 g/cm^3). Sub-samples were homogenized and weighed into 10 mL glass vials and kept frozen at -20°C prior to subsequent analysis.

Selective extractions

The soil layers were subjected to several chemical extractions to quantify the different iron phases. The soils were kept frozen prior to analysis, then dried at 20°C under anoxic conditions until no further weight loss was observed (1 day). 0.3 g dry soil was weighed into a 10 mL glass vial with 6.25 mL extractant and N_2 headspace. Prior to use, all glassware was washed with 1 M HCl for 10 min, flushed three times with deionized water and once with MilliQ water. Afterwards glassware was sterilized at 180°C in the oven for 4.5 hours. All samples were centrifuged at room temperature for 10 min at 5300 g. After centrifugation the supernatant was decanted into another 10 mL glass vial. Each extraction was performed in duplicates for each layer. Throughout the extraction, samples were kept in the dark under anoxic conditions (N_2 atmosphere). The extracts were analyzed for Fe and DOC as described above. Additionally, the samples were acidified in 1% (v/v) HNO_3 and analyzed in duplicates by MP-AES/ICP-MS to get the total Fe, S, P and Al concentrations (S3 and S4). The illustrated iron values throughout the whole study represent the iron values obtained by the ferrozine assay (for differences in iron concentrations through the different analysis see S3). Due to dark color of the extracts which can disturb the spectrophotometric measurement during ferrozine complexation, the absorbance of blanks (sample diluted in 1 M HCl or hydroxylamine-HCl) was measured and later subtracted to avoid overestimation of iron concentrations. All Fe analysis (ferrozine assay, MP-AES/ICP-MS analysis) show the same iron trends with depth and along the thaw gradient (S3). For additional extractant specific experimental parameters see below.

6 M HCl

To quantify the total extractable Fe of the soil layers, dried samples were subjected to a 70°C 6 M HCl extraction for 24 h[46,47].

Sodium pyrophosphate

The sodium pyrophosphate extraction was performed following Coward *et al* (2017)[2] at pH 10 to determine the colloidal or OM-chelated iron.

Hydroxylamine-HCl

To extract the short ranged ordered (SRO) Fe oxides, an acidic hydroxylamine-HCl (pH <2) extraction was carried out under the same conditions as the sodium pyrophosphate extraction[2].

Dithionite-citrate

Extractions were conducted using a solution of 0.27 M trisodium citrate, 0.11 M sodium bicarbonate and 0.1 M sodium dithionite (total ionic strength: 1.85 M), as previously described[4] (S2). This extraction was used to also quantify the reactive iron minerals but in particular the organic molecules binding to it (released during iron mineral dissolution). Instead of heating to 80°C as described by Lalonde *et al* (2012)[4], the dithionite-citrate extraction was performed under the same conditions as the sodium pyrophosphate and hydroxylamine-HCl extraction (on a rolling shaker at room temperature for 16h) for better comparison between the different extractions. The citrate addition as a metal ion complexing agent was necessary to avoid under-estimation of iron and organic carbon as a result of complexation or mineral precipitation during extraction (S2). Without citrate addition, we obtained 64±3% less iron and 57±28% less carbon after sodium dithionite reductive dissolution. As described in Lalonde *et al* (2012)[4], we also used a 1.85 M sodium chloride/0.11 M sodium bicarbonate extraction as a control experiment under the same conditions (same solid:solution ratio, temperature, time, ionic strength) to distinguish between organic carbon (OC) which is readily desorbed and organic carbon which is released by the reduction of iron(III) minerals (S2). To determine the DOC background concentrations caused by the trisodium citrate, blanks (trisodium citrate sodium bicarbonate solution) were analyzed during each measurement. The background concentration was later subtracted from the total DOC value, as well as the DOC concentration of the control

experiment (sodium chloride sodium bicarbonate solution), resulting in the OC which is released by the reduction of reactive iron (Table S1, S2).

TOC analysis

To quantify the total organic carbon (TOC) (Fig. 4, Table S1, Fig. S6 and Fig. S8), soil samples from each layer were dried at 60°C until the weight remained constant. The dry soils were then ground and acidified with 16% HCl to remove the inorganic carbon. After washing with deionized water and subsequent drying, the TOC content was analyzed by an Elementar vario El (Elementar Analysensysteme GmbH, Germany). The TOC content goes in line with previously reported values [48-50].

EXAFS/XANES analysis

Samples were dried under N_2 atmosphere and stored anoxically in a glove box prior to analysis. Sample were then sealed in plastic multi-sample holders with Kapton polyimide tape and kept anoxic until they were transferred to a sample mount at the beamline. The sample holder was in a cryostat during analysis to limit beam damage and to prevent oxidation of Fe(II). Reference samples such as natural nontronite and ferrosmectite (referred to as Fe clays) were obtained from the Clay Mineral Society. Fe(II)-citrate and Fe(III)-citrate were used as reference samples for Fe(II)-OM and Fe(III)-OM, and were prepared and analysed as described in Daugherty *et al* (2017)[51]. Mackinawite, used as a reference for FeS, was prepared and analysed as described in Troyer *et al* (2014)[52]. 2-line ferrihydrite, prepared and analysed as described in Borch *et al* (2007)[53], was used as a reference for poorly crystalline Fe (Fig. 3).

Fe K-edge X-ray absorption spectroscopic analyses were conducted at Beamline 11−2 at the Stanford Synchrotron Radiation Light source (SSRL) in Menlo Park, CA. The Si(220) phi = 0° monochromator was used, and beam size of 1 mm vertical and 10 mm horizontal. Iron X-ray absorption near edge structure (XANES) and EXAFS fluorescence spectra were collected with the PIPS detector simultaneously with the transmission spectrum of Fe foil, which was used for

internal energy calibrations. Multiple scans (3-4) per sample were acquired as necessary to achieve satisfactory data quality.

Scans were calibrated to 7112 eV (the first inflection point of Fe(0), and then averaged over 3 or 4 scans using SixPack software. They were deglitched at 7250 and 7600 eV, and then normalized with the E0 value, determined by finding the inflection point of the first derivative of each sample. Linear combination fitting (LCF) of EXAFS spectra was performed in SixPack from chi values of 2 to 12 with an x-weight of 3. Non-negative fits were performed, and components were chosen based on prior knowledge of the sample mineralogy.

Correlative SEM and nanoSIMS

The two end-members, palsa and fen, were analyzed using SEM and nanoSIMS (Fig. 4, Fig. S9) using only the free particles of the fine fraction of the transition zone and the mineral horizon. As described by Kopittke *et al* (2018)[54] and Keiluweit *et al* (2012)[55], subsamples of each layer (1 mg) were dispersed in 10 mL of anoxic deionized water and gently shaken to obtain the free organo-mineral particles from the fine fraction of the soil. 100 µl of the suspension was placed onto a silica wafer and dried under N_2 atmosphere. The samples were sputter-coated with 12 nm platinum (Pt) using a Bal-Tec SCD005 sputter coater.

To characterize the organo-mineral particles of the fine fraction by size and crystallinity and identify representative particles, a field emission scanning electron microscope (FE-SEM; Jeol JSM-6500F), equipped with secondary electron detector, was used prior to nanoSIMS analysis. The acceleration voltage was set to 5 kV with a working distance of 10 mm.

The nanoSIMS analyses were performed at the Cameca nanoSIMS 50L of the Chair of Soil Science (TU München, Germany). Prior to the measurements, the samples were additionally coated with Au/Pd layer (~30 nm) to avoid charging during the analysis. The Cs^+ primary ion beam was used with a primary ion impact energy of 16 keV. Prior to the final measurement, any potential contaminants and the Au/Pd coating layer were sputtered away at 50 x 50 µm

with a high primary beam current (pre-sputtering). To enhance the secondary ion yields, Cs^+ ions were implanted into the sample during this pre-sputtering process. The primary beam (~1.2 pA) was focused at a lateral resolution ~100 nm and scanned over the sample with $^{12}C^-$, $^{16}O^-$, $^{12}C^{14}N^-$, $^{31}P^-$, $^{32}S^-$, $^{27}Al^{16}O^-$ and $^{56}Fe^{16}O^-$ secondary ions collected using electron multipliers. To compensate for any charging of the non-conductive mineral particles, the electron flood gun was used. All analyses were performed in imaging mode. For every layer, four representative spots were analyzed to obtain a reliable data basis for the spatial distribution of $^{12}C^-$ and $^{56}Fe^{16}O^-$. Ion images of 30 x 30 µm field of view, 30 planes with a dwell time of 1 ms/pixel, 256 pixels x 256 pixels were recorded. The estimated depth resolution with 16 keV Cs^+ ions was 10 nm. Finally, the nanoSIMS images were analyzed using the Open MIMS Image plugin available within ImageJ (available free-of-charge at, https:// imagej.nih.gov/ij/). All presented images were corrected for the electron multiplier dead time (44 ns), as well as drift corrected, and the planes accumulated. A median filter was applied on all images.

Most probable number (MPN) counts

A growth-dependent approach, most probable number (MPN) counts (Fig. 2), was performed on the soil samples from the different depths of the cores in seven replicates. This is a useful way to quantify Fe(III)-metabolizing bacteria as there is a lack of specificity in the potential genes used for Fe(III) reduction and has the strength of directly showing that the microorganisms are capable of reducing Fe(III). MPNs were set up in 96-well plates with soil dilutions in liquid media for quantification of Fe(III)-reducing bacteria[56,57]. 5 mM sodium acetate, 5 mM sodium lactate and 5 mM 2-line ferrihydrite (chemically synthesized as previously described[57]) were added to the anoxic media (0.6 g/L KH_2PO_4, 0.3 g/L NH_4Cl, 0.025 g/L$MgSO_4$ x 7 H_20, 0.4 g/L $MgCl_2$ x 6 H_20, $CaCl_2$ x 2 H_20, 22 mM $NaHCO_3$, 1 mL/L trace element according to Widdel et al (1983)[58], 1 mL/L vitamin solution after Widdel & Pfennig (1981)[59] and 1 mL/L selenite/tungstate solution according to Widdel (1980)[60]). To calculate the

cell numbers (cells/g soil) from the positive MPN wells, the software program KLEE was used applying confidence limits of Cornish and Fisher (1938)[61] and the bias correction after Salam (1978)[62,63]. Further isolation of Fe(III)-reducing bacteria was performed with same media and supplies via multiple round of serial dilution. DNA was extracted of the further isolated culture (after 7 transfers) using the UltraClean® Microbial DNA Isolation Kit (MO BIO Labratories, Carlsbad, CA, US). 16S rRNA gene fragments were amplified using the 341F (CCTACGGGAGGCAGCAG) and 907R (CCGTCAATTCCTTTRAGTTT) primer pair[64] and resulting amplicons were sent for Sanger sequencing (Eurofins GATC biotech, Konstanz, Germany). Sequence results were analyzed using nucleotide BLAST (Basic Local Alignment Search Tool) to identify the closest relatives of both microbial partners.

References

1 Shimizu, M. *et al.* Dissimilatory Reduction and Transformation of Ferrihydrite-Humic Acid Coprecipitates. *Environ Sci Technol* **47**, 13375-13384 (2013).

2 Coward, E. K., Thompson, A. T. & Plante, A. F. Iron-mediated mineralogical control of organic matter accumulation in tropical soils. *Geoderma* **306**, 206-216 (2017).

3 Kleber, M., Mikutta, R., Torn, M. S. & Jahn, R. Poorly crystalline mineral phases protect organic matter in acid subsoil horizons. *Eur J Soil Sci* **56**, 717-725 (2005).

4 Lalonde, K., Mucci, A., Ouellet, A. & Gelinas, Y. Preservation of organic matter in sediments promoted by iron. *Nature* **483**, 198-200 (2012).

5 Riedel, T., Zak, D., Biester, H. & Dittmar, T. Iron traps terrestrially derived dissolved organic matter at redox interfaces. *P Natl Acad Sci USA* **110**, 10101-10105 (2013).

6 Herndon, E. M. *et al.* Pathways of anaerobic organic matter decomposition in tundra soils from Barrow, Alaska. *J Geophys Res-Biogeo* **120**, 2345-2359 (2015).

7 Lipson, D. A., Jha, M., Raab, T. K. & Oechel, W. C. Reduction of iron (III) and humic substances plays a major role in anaerobic respiration in an Arctic peat soil. *J Geophys Res-Biogeo* **115,** G00I06 (2010).

8 Olefeldt, D., Turetsky, M. R., Crill, P. M. & McGuire, A. D. Environmental and physical controls on northern terrestrial methane emissions across permafrost zones. *Global Change Biol* **19**, 589-603 (2013).

9 Turetsky, M. R. *et al.* Short-term response of methane fluxes and methanogen activity to water table and soil warming manipulations in an Alaskan peatland. *J Geophys Res-Biogeo* **113**, G000496 (2008).

10 Zona, D. *et al.* Methane fluxes during the initiation of a large-scale water table manipulation experiment in the Alaskan Arctic tundra. *Global Biogeochem Cy* **23**, GB2013 (2009).

11 Malmer, N., Johansson, T., Olsrud, M. & Christensen, T. R. Vegetation, climatic changes and net carbon sequestration in a North-Scandinavian subarctic mire over 30 years. *Global Change Biol* **11**, 1895-1909 (2005).

12 Hodgkins, S. B. *et al.* Changes in peat chemistry associated with permafrost thaw increase greenhouse gas production. *P Natl Acad Sci USA* **111**, 5819-5824 (2014).

13 Johansson, T. *et al.* Decadal vegetation changes in a northern peatland, greenhouse gas fluxes and net radiative forcing. *Global Change Biol* **12**, 2352-2369 (2006).

14 Swindles, G. T. *et al.* The long-term fate of permafrost peatlands under rapid climate warming. *Sci Rep* **5**, 17951 (2015).

15 McCalley, C. K. *et al.* Methane dynamics regulated by microbial community response to permafrost thaw. *Nature* **514**, 478-481 (2014).

16 Woodcroft, B. J. *et al.* Genome-centric view of carbon processing in thawing permafrost. *Nature* **560**, 49-54 (2018).

17 Rydén, B. E., Fors, L & Kostov, L. Physical properties of the tundra soil-water system at Stordalen, Abisko. *Ecol Bull* **30**, 27-54 (1980).

18 Janssen, P. J. *et al.* The complete genome sequence of Cupriavidus metallidurans strain CH34, a master survivalist in harsh and anthropogenic environments. *PLoS One* **5**, e10433 (2010).

19 Reiche, M., Torburg, G. & Küsel, K. Competition of Fe(III) reduction and methanogenesis in an acidic fen. *FEMS Microbiol Ecol* **65**, 88-101 (2008).

20 Mehra, O. P. & Jackson, M. L. Iron oxide removal from soils and clays by a dithionite-citrate system buffered with sodium bicarbonate. *Clays Clay Min.* **7**, 317-327 (1958).

21 Mu, C. C. *et al.* Soil organic carbon stabilization by iron in permafrost regions of the Qinghai-Tibet Plateau. *Geophys Res Lett* **43**, 10286-10294 (2016).

22 Herndon, E. M. *et al*. Iron (oxyhydr)oxides serve as phosphate traps in tundra and boreal peat soils. *J Geophys Res-Biogeo* **124**, G004776 (2019).

23 Sowers, T. D. *et al*. Spatially-resolved organomineral interactions across a permafrost chronosequence. *Environ Sci Technol* **54**, 2951-2960 (2020).

24 Wagai, R. & Mayer, L. M. Sorptive stabilization of organic matter in soils by hydrous iron oxides. *Geochim Cosmochim Ac* **71**, 25-35 (2007).

25 Herndon, E. M. *et al*. Influence of iron redox cycling on organo-mineral associations in Arctic tundra soil. *Geochim Cosmochim Ac* **207**, 210-231 (2017).

26 Mu, C. C. *et al*. Organic carbon stabilized by iron during slump deformation on the Qinghai- Tibetan Plateau. *Catena* **187**, 104282 (2020).

27 Tarnocai, C. *et al.* Soil organic carbon pools in the northern circumpolar permafrost region. *Global Biogeochem Cy* **23**, GB2023 (2009).

28 Van Bodegom, P. M., Scholten, J. C. M. & Stams, A. J. M. Direct inhibition of methanogenesis by ferric iron. *FEMS Microbiol Ecol* **49**, 261-268 (2004).

29 Wagner, R., Zona, D., Oechel, W. & Lipson, D. Microbial community structure and soil pH correspond to methane production in Arctic Alaska soils. *Method Enzymol* **19**, 3398-3410 (2017).

30 Prakash, D., Chauhan, S. S. & Ferry, J. G. Life on the thermodynamic edge : Respiratory growth of an acetotrophic methanogen. *Sci Adv* **5**, eaaw9059 (2019).

31 Perryman, C. R. *et al*. Thaw Transitions and Redox Conditions Drive Methane Oxidation in a Permafrost Peatland. *J Geophys Res-Biogeo* **125**, G005526 (2020).

32 Pokrovsky, O. S., Manasypov, R. M., Loiko, S. V. & Shirokova, L. S. Organic and organo-mineral colloids in discontinuous permafrost zone. *Geochim Cosmochim Ac* **188**, 1-20 (2016).

33 Mondav, R. *et al.* Discovery of a novel methanogen prevalent in thawing permafrost. *Nat Commun* **5**, 3212 (2014).

34 Akerman, H. J. & Johansson, M. Thawing permafrost and thicker active layers in sub-arctic Sweden. *Permafrost Periglac* **19**, 279-292 (2008).

35 Klaminder, J., Yoo, K., Rydberg, J. & Giesler, R. An explorative study of mercury export from a thawing palsa mire. *J Geophys Res-Biogeo* **113**, G000776 (2008).

36 Callaghan, T. V. *et al.* A new climate era in the sub-Arctic: Accelerating climate changes and multiple impacts. *Geophys Res Lett* **37**, L14705 (2010).

37 Jorgenson, M. T., Racine, C. H., Walters, J. C. & Osterkamp, T. E. Permafrost degradation and ecological changes associated with a warming climate in central Alaska. *Climatic Change* **48**, 551-579 (2001).

38 O'Donnell, J. A. *et al.* The Effects of Permafrost Thaw on Soil Hydrologic, Thermal, and Carbon Dynamics in an Alaskan Peatland. *Ecosystems* **15**, 213-229 (2012).

39 Payette, S., Delwaide, A., Caccianiga, M. & Beauchemin, M. Accelerated thawing of subarctic peatland permafrost over the last 50 years. *Geophys Res Lett* **31**, GL020358 (2004).

40 Vitt, D. H., Halsey, L. A. & Zoltai, S. C. The changing landscape of Canada's western boreal forest: the current dynamics of permafrost. *Can J Forest Res* **30**, 283-287 (2000).

41 Quinton, W. L., Hayashi, M. & Chasmer, L. E. Permafrost-thaw-induced land-cover change in the Canadian subarctic: implications for water resources. *Hydrol Process* **25**, 152-158 (2011).

42 Zoltai, S. C. Cyclic Development of Permafrost in the Peatlands of Northwestern Alberta, Canada. *Arctic Alpine Res* **25**, 240-246 (1993).

43 Olefeldt, D. & Roulet, N. T. Effects of permafrost and hydrology on the composition and transport of dissolved organic carbon in a subarctic peatland complex. *J Geophys Res-Biogeo* **117**, G01005 (2012).

44 Stookey, L. L. Ferrozine - a New Spectrophotometric Reagent for Iron. *Anal Chem* **42**, 779-781 (1970).

45 Bockheim, J. G., Hinkel, K. M. & Nelson, F. E. Predicting carbon storage in tundra soils of arctic Alaska. *Soil Sci Soc Am J* **67**, 948-950 (2003).

46 Aller, R. C., Mackin, J. E. & Cox, R. T. Diagenesis of Fe and S in Amazon Inner Shelf Muds - Apparent Dominance of Fe Reduction and Implications for the Genesis of Ironstones. *Cont Shelf Res* **6**, 263-289 (1986).

47 Poulton, S. W. & Canfield, D. E. Development of a sequential extraction procedure for iron: implications for iron partitioning in continentally derived particulates. *Chem Geol* **214**, 209-221 (2005).

48 Lupascu, M., Wadham, J. L., Hornibrook, E. R. C. & Pancost, R. D. Temperature Sensitivity of Methane Production in the Permafrost Active Layer at Stordalen, Sweden: a Comparison with Non-permafrost Northern Wetlands. *Arct Antarct Alp Res* **44**, 469-482 (2012).

49 Siewert, M. B. High-resolution digital mapping of soil organic carbon in permafrost terrain using machine learning: a case study in a sub-Arctic peatland environment. *Biogeosciences* **15**, 1663-1682 (2018).

50 Hugelius, G. *et al*. Estimated stocks of circumpolar permafrost carbon with quantified uncertainty ranges and identified data gaps. *Biogeosciences* **11**, 6573-6593 (2014).

51 Daugherty, E. E., Gilbert, B., Nico, P. S. & Borch, T. Complexation and Redox Buffering of Iron(II) by Dissolved Organic Matter. *Environ Sci Technol* **51**, 11096-11104 (2017).

52 Troyer, L. D., Tang, Y. & Borch, T. Simultaneous reduction of arsenic(V) and uranium(VI) by mackinawite: role of uranyl arsenate precipitate formation. *Environ Sci Technol* **48**, 14326-14334 (2014).

53 Borch, T., Masue, Y., Kukkadapu, R. K. & Fendorf, S. Phosphate imposed limitations on biological reduction and alteration of ferrihydrite. *Environ Sci Technol* **41**, 166-172 (2007).

54 Kopittke, P. M. *et al.* Nitrogen-rich microbial products provide new organo-mineral associations for the stabilization of soil organic matter. *Global Change Biol* **24**, 1762-1770 (2018).

55 Keiluweit, M. *et al.* Nano-scale investigation of the association of microbial nitrogen residues with iron (hydr)oxides in a forest soil O-horizon. *Geochim Cosmochim Ac* **95**, 213-226 (2012).

56 Melton, E. D., Rudolph, A., Behrens, S., Schmidt, C. & Kappler, A. Influence of Nutrient Concentrations on MPN Quantification and Enrichment of Nitrate-Reducing Fe(II)-Oxidizing and Fe(III)-Reducing Bacteria from Littoral Freshwater Lake Sediments. *Geomicrobiol J* **31**, 788-801 (2014).

57 Straub, K. L., Kappler, A. & Schink, B. Enrichment and isolation of ferric-iron- and humic-acid-reducing bacteria. *Method Enzymol* **397**, 58-77 (2005).

58 Widdel, F., Kohring, G. W. & Mayer, F. Studies on Dissimilatory Sulfate-Reducing Bacteria That Decompose Fatty-Acids .3. Characterization of the Filamentous Gliding Desulfonema-Limicola Gen-Nov Sp-Nov, and Desulfonema-Magnum Sp-Nov. *Arch Microbiol* **134**, 286-294 (1983).

59 Widdel, F. & Pfennig, N. Studies on Dissimilatory Sulfate-Reducing Bacteria That Decompose Fatty-Acids .1. Isolation of New Sulfate-Reducing Bacteria Enriched with

Acetate from Saline Environments - Description of Desulfobacter-Postgatei Gen-Nov, Sp-Nov. *Arch Microbiol* **129**, 395-400 (1981).

60 Widdel, F. Anaerobic degradation of fatty acids and benzoic acid by newly isolated species sulphate-reducing bacteria. *Dissertation, Universität Göttingen, FRG* (1980).

61 Cornish, E. A. & Fisher, R. A. Moments and cumulants in the specification of distributions. *Revue de l'Institut International de Statistique/Rev. Int. Stat. Inst. 5* **4**, 307-320 (1938).

62 Klee, A. J. A Computer-Program for the Determination of Most Probable Number and Its Confidence-Limits. *J Microbiol Meth* **18**, 91-98 (1993).

63 Salama, I. A., Koch, G. G. & Tolley, H. D. On the estimation of the most probable number in a serial dilution technique. *Commun. Stat. - Theory Methods* **A7**, 1267-1281 (1978).

64 Muyzer, G., de Waal, E. C. & Uitterlinden, A. G. Profiling of complex microbial populations by denaturing gradient gel electrophoresis analysis of polymerase chain reaction-amplified genes coding for 16S rRNA. *Appl Environ Microbio* **59**, 659-700 (1993).

Acknowledgements

The authors would like to acknowledge the Abisko Research Station (Abisko, Sweden) for their support during sampling missions. We thank H. Miller (Colorado State University, Fort Collins, United States) for her assistance with EXAFS analysis, G. Harrington and J. Lugmeier (Munich, Germany) for nanoSIMS analysis and E. Stopelli (Zuerich, Switzerland) for ICP-MS measurements. This work was supported by the University of Tübingen (Programme for the Promotion of Junior Researchers grant to C.B) and by the German Academic Scholar Foundation (scholarship to M.P). Use of the Stanford Synchrotron Radiation Lightsource, SLAC National Accelerator Laboratory, is supported by the U.S. Department of Energy, Office of Science, Office of Basic Energy Sciences under Contract No. DE-AC02-76SF00515.

Author information

Affiliations

Geomicrobiology, Center for Applied Geosciences, University of Tuebingen, Sigwartstrasse 10, 72076 Tuebingen, Germany

Monique S. Patzner, Miroslava Malusova, Moritz Baur, Verena Nikeleit, James M. Byrne, Andreas Kappler & Casey Bryce

Lehrstuhl für Bodenkunde, Technische Universitaet Muenchen, Emil-Ramann Strasse 2, 85354, Freising, Germany

Carsten W. Mueller, Carmen Hoeschen

Department of Geosciences and Natural Resource Management, University of Copenhagen, Øster Voldgade 10, 1350 København K, Denmark

Carsten W. Mueller

Soil Science and Geomorphology, University of Tuebingen, Ruemelinstraße 19-23, 72070 Tuebingen, Germany

Thomas Scholten

Department of Soil & Crop Sciences, Colorado State University, 307 University Ave, 80523-1170, Fort Collins, US

Thomas Borch

School of Earth Sciences, University of Bristol, Wills Memorial Building, Queens Road BS8 1RJ, Bristol, UK

James M. Byrne, Casey Bryce

Contributions

The original hypothesis was formulated by C.B and A.K. M.P, C.B and A.K designed the project, interpreted the data and wrote the manuscript. M.P, C.B and M.M collected the samples. M.P gathered the data presented in the main text. Supporting information from the

2017 campaign was collected by V.N, M.M, M.B. and C.B. T.B conducted the synchrotron analysis and contributed to the data analysis and interpretation. C. H. and C.W.M, together with M.P, collected, analyzed and interpreted the nanoSIMS data. J.B and M.P conducted the SEM analyses. T.S contributed to project design and data interpretation. All authors contributed to the preparation of the manuscript.

Competing interests

The authors declare no competing financial interests.

Corresponding author

Correspondence to Casey Bryce, School of Earth Sciences, University of Bristol

casey.bryce@bristol.ac.uk

Supplementary Information for

Iron mineral dissolution releases iron and associated organic carbon during permafrost thaw

Monique S. Patzner[1], Carsten W. Mueller[2,3], Miroslava Malusova[1], Moritz Baur[1], Verena Nikeleit[1], Thomas Scholten[4], Carmen Hoeschen[2], James M. Byrne[1], Thomas Borch[5], Andreas Kappler[1] & Casey Bryce[1,6]*

* Casey Bryce

Email: casey.bryce@bristol.ac.uk

S1. Absolute and % values of organic carbon and reactive iron reported in the main text

	Reactive iron (control corrected)	Reactive iron of total extractable iron	Control iron	C bound to reactive iron (control corrected)	C bound to reactive iron of the total organic carbon	Control carbon	OC:Fe	Total organic carbon	Total extractable Fe
	mg/g	%	mg/g	mg/g	%	mg/g		mg/g	mg/g
Palsa A									
Organic horizon	0.40 ± 0.11	100.00	0.00 ± 0.00	0.94 ± 0.58	0.22	1.37 ± 0.01	2.35	423 ± 0.00	0.20 ± 0.02
	0.29 ± 0.09	100.00	0.00 ± 0.00	2.16 ± 0.95	0.51	1.65 ± 0.08	7.45	422.91 ± 0.13	0.17 ± 0.00
Transition zone	2.55 ± 0.57	72.86	0.29 ± 0.08	30.99 ± 0.71	9.93	3.13 ± 0.02	12.15	312.11 ± 0.33	3.51 ± 0.08
	8.44 ± 0.21	93.86	0.75 ± 0.11	52.50 ± 0.13	14.80	10.36 ± 0.50	6.22	354.72 ± 0.04	8.99 ± 0.28
Mineral horizon	3.17 ± 0.19	36.58	0.25 ± 0.03	27.39 ± 1.61	20.13	2.88 ± 0.08	8.64	136.11 ± 0.21	8.65 ± 0.28
	1.35 ± 0.21	10.00	0.07 ± 0.06	13.58 ± 0.42	18.67	1.39 ± 0.10	10.06	72.71 ± 0.29	13.48 ± 0.22
Bog C									
Organic horizon	1.48 ± 0.18	40.60	0.73 ± 0.07	16.16 ± 3.91	4.85	3.16 ± 1.67	10.92	333.31 ± 0.05	3.63 ± 0.05
Transition zone	2.08 ± 0.05	11.14	0.41 ± 0.04	22.67 ± 8.60	39.42	1.18 ± 0.21	10.90	57.51 ± 0.38	18.65 ± 0.70
Mineral horizon	0.88 ± 0.06	7.52	0.28 ± 0.04	0.00 ± 0.00	0.00	1.04 ± 0.01	0.00	8.28 ± 0.25	11.69 ± 0.81
Fen E									
Organic horizon	2.03 ± 0.14	43.39	0.75 ± 0.00	0.00 ± 0.00	0.00	1.53 ± 0.00	0.00	234.70 ± 0.83	4.68 ± 0.01
Transition zone	2.64 ± 0.03	18.29	0.37 ± 0.00	0.00 ± 0.00	0.00	1.38 ± 0.18	0.00	16.24 ± 0.18	14.46 ± 0.22
Mineral horizon	1.75 ± 0.04	10.71	0.15 ± 0.00	0.00 ± 0.00	0.00	2.57 ± 0.76	0.00	3.52 ± 0.05	16.34 ± 0.44
	1.70 ± 0.04	8.95	0.19 ± 0.01	0.00 ± 0.00	0.00	1.13 ± 0.17	0.00	4.99 ± 0.10	19.01 ± 0.25

Table S1. Absolute and % values of iron and carbon in locations Palsa A, Bog C and Fen E, i.e. the cores reported in the main text. In most of the layers, the maximum molar ratio of organic carbon to iron exceeds 1.0, the maximal sorption capacity of reactive iron oxides for natural organic matter[24]. Co-precipitation and/or chelation of organic compounds can generate structures with OC:Fe ratios of up to 6 to 10, as shown in other studies[24]. Errors indicate the range of duplicate analyses of each layer in each thaw stage.

S2. Fe-associated organic carbon: extraction method and controls

The determination of Fe-associated organic carbon has several well-known difficulties which can only be addressed by combining different approaches.

Considerations for the sodium dithionite-citrate extraction:

(1) pH

To prevent hydrolysis of organic matter as well as its protonation and re-adsorption onto sediment particles, which occur under acidic conditions, the sodium dithionite citrate extraction was performed at circumneutral pH (sodium bicarbonate buffered). Therefore, the additional hydroxylamine-HCl extraction (performed below pH 2) can only be a comparison for the sodium dithionite citrate extractable Fe, but not for the sodium dithionite citrate extractable carbon. The control extraction was performed under the same ionic strength (addition of NaCl) and pH (sodium bicarbonate buffered).

(2) Leaching of carbon which is not associated with iron

The carbon measured in the sodium dithionite citrate extraction was corrected by subtraction of the measured DOC values in a citrate blank and in a control extraction, performed under the same ionic strength and pH. This control extraction determines how much carbon would be leached from the soil without any reduction (see Table S1 and Figure S1). The effect of a reducing agent, which potentially reductively transforms certain organic functional groups, is not considered in this control (see point *(3)*).

(3) Dithionite as strong reducing agent

Dithionite is a strong reducing agent which can reductively transform certain organic functional groups and could lead to organic carbon release which is not associated with reactive Fe. Nevertheless, we consider this to be negligible for our extractions as the concentration of sodium dithionite citrate extractable carbon of a horizon containing primarily organic material and no mineral phase (Palsa A, organic horizon) is very low (0.3±0.1 to 0.4±0.1 mg extractable carbon

per g soil; see also Table S1). Additionally, a sodium pyrophosphate extraction was performed to determine the colloidal/OM-Fe. The sodium pyrophosphate extraction carbon yielded similar concentrations and showed similar trends to the dithionite-citrate extractable carbon across the thaw gradient (Figure S1). Variation between the absolute values can occur due to heterogeneity in the samples and the alkaline conditions of the sodium pyrophosphate extraction (pH 10).

(4) Citrate as strong metal complexing agent

Citrate is a strong metal complexing agent that can influence the amount of extractable iron during dithionite extraction. A test-run was performed with the same experimental conditions (same ionic strength and pH), but no citrate addition. Without citrate, we obtained 64±3% less iron and 57±28% less carbon after sodium dithionite reductive dissolution. We therefore concluded, that the metal ion complexing agent citrate is necessary to avoid under-estimation of iron and organic carbon as a result of complexing or mineral precipitation during extraction.

Since extractions have well-known limitations as mentioned above, additional approaches were used and combined to characterize Fe-C associations in the solid phase along the thaw gradient.

<u>Additional approaches used were:</u>

(A) Extended X-ray absorption fine structure (EXAFS) with reference for reactive Fe (ferrihydrite) and references for organic carbon associated with Fe (Fe(II)-citrate) and Fe(III)-citrate)

(B) Nanoscale analysis using correlative SEM and nanoSIMS to show close spatial distribution of iron and carbon

The data set is consistent with an increase in aqueous Fe^{2+} and DOC and an increasing abundance of Fe(III)-reducing bacteria along the thaw gradient.

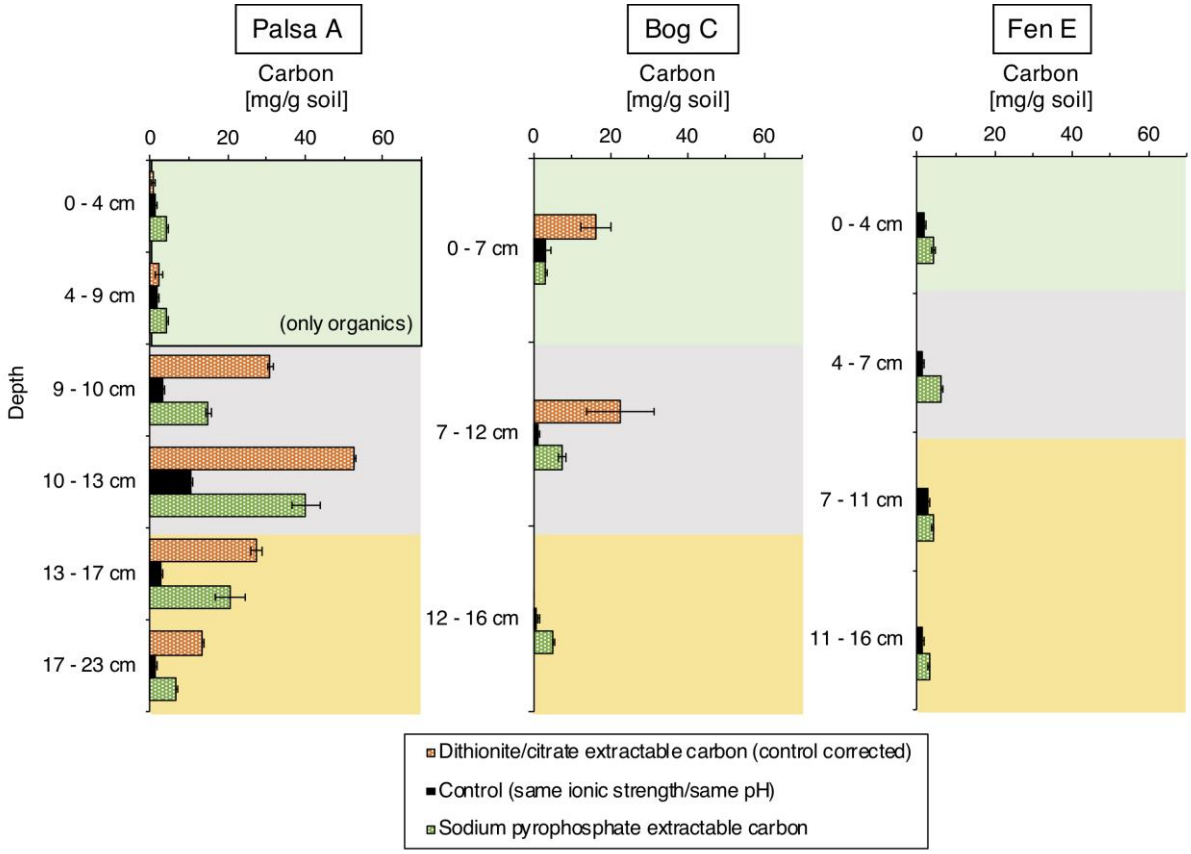

Figure S1. Extractable carbon measured using different approaches to address issues with the sodium dithionite citrate extraction. The sodium dithionite citrate extractable carbon is control corrected (subtraction of citrate blank and extractable carbon of the control extraction with same ionic strength and pH), shown in orange (see also Table S1). The control extraction (same ionic strength and pH) is shown in black (see also Table S1). The sodium pyrophosphate (pH 10) extractable carbon shows similar amounts and trends with depth and along the thaw gradient, as the control corrected dithionite citrate extractable carbon. Dithionite citrate extractable carbon only from organics (Box, Palsa A, organic horizon) is low, therefore hydrolytic cleavage of organic matter can be ruled out.

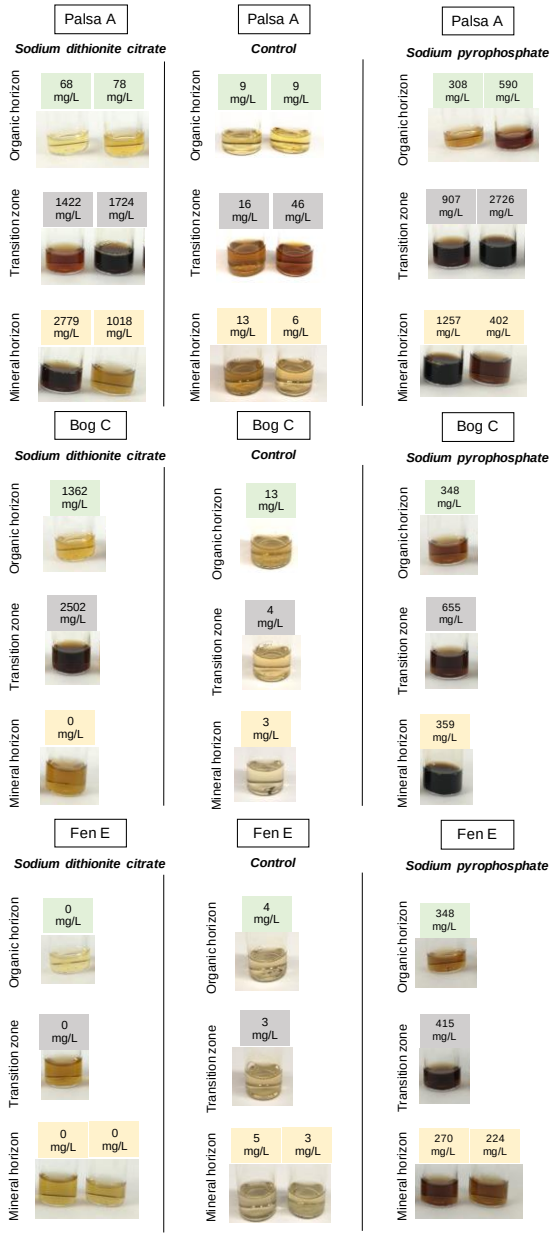

Figure S2. Extracts of sodium dithionite, control and sodium pyrophosphate. Values of sodium dithionite citrate indicate the dissolved organic carbon concentrations in the extracts after subtraction of the background of the citrate concentration. The background concentration of the citrate for the analysis Palsa A, Bog C and Fen F was 20.5±0.14g/L. Pictures of the extracts are shown to highlight the loss of the reactive iron phase and carbon associated with it along the thaw gradient, here visible by brown color loss in the sodium dithionite citrate extracts from palsa to fen. The control is shown to demonstrate that there was no carbon leached under same ionic strength and pH. The sodium pyrophosphate extracts support the trends shown by the sodium dithionite citrate extraction. Green marks the organic horizon, grey the transition zone and yellow the mineral horizon.

S3. Different Fe analysis of the extracts to rule out matrix effects

Different analytical approaches (ferrozine assay, MP-AES, ICP-MS) have been used to determine Fe in the extracts, to rule out matrix effects and to determine additional elements in the extracts. ICP-MS was also used to measure sulphur (S) and phosphorous (P) (Figure S4). MP-AES was also used to determine aluminum concentrations in the extracts (Al) (Figure S4). We are aware of differences between the iron values. However, because the values only vary slightly and sodium dithionite citrate was not measured with ICP-MS and MP-AES due to citric formation after acidification, we decided to use the data from the ferrozine assay.

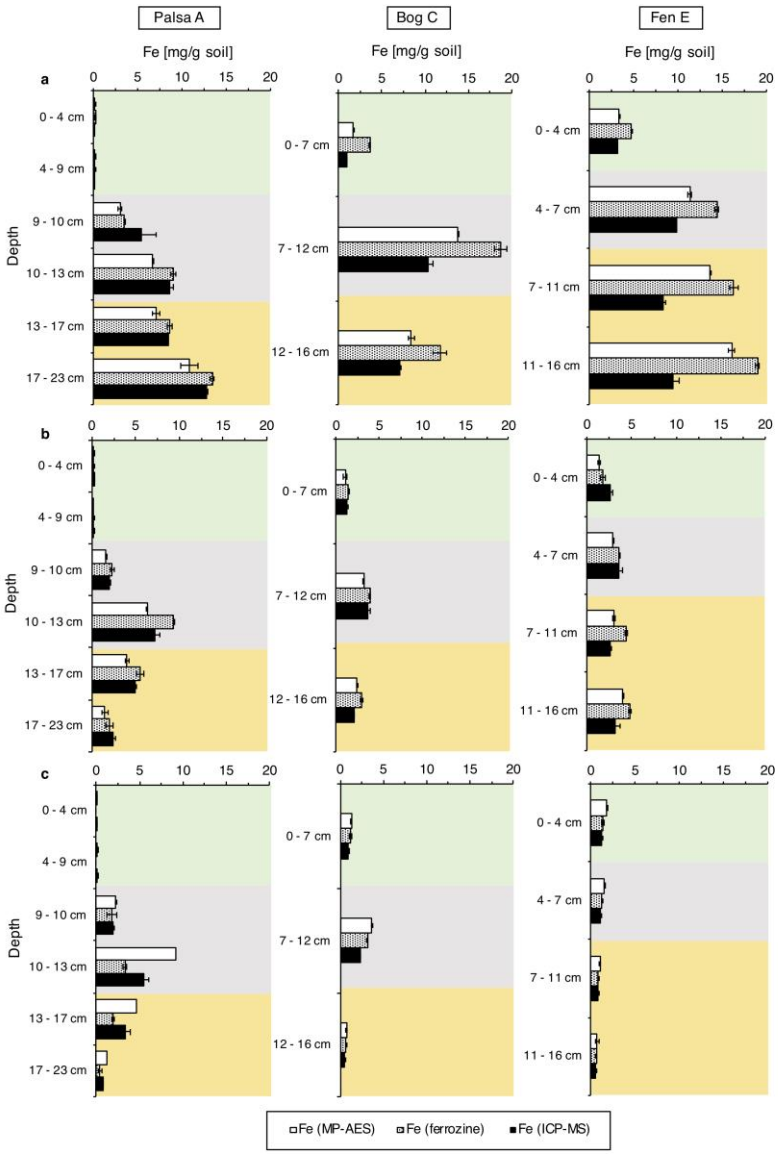

Figure S3. Fe analysis by MP-AES, ferrozine and ICP-MS analysis of Palsa A, Bog C and Fen E: a, 6M HCl extraction, b, hydroxylamine-HCl extraction and c, sodium pyrophosphate extraction. Due to citric acid formation after acidification, the sodium dithionite citrate extract was not measured with the more sensitive MP-AES and ICP-MS instrument. For the 6M HCl and hydroxylamine-HCl extracts, the MP-AES iron values are slightly lower than the ferrozine iron values due to matrix interference during MP-AES measurements of the extracts (HCl). For the sodium pyrophosphate extract, the MP-AES iron values are slightly higher than the ferrozine iron values. This could be explained by the dark color of the extracts which disturb the spectrophotometric measurement during ferrozine complexation. After blank subtraction this can result in lower iron concentrations determined by the ferrozine assay. The ICP-MS iron values are close to the ferrozine values (122±54% similarity), except for one extraction (6M HCl extraction) and two horizons (transition zone and mineral horizon of bog and fen).

S4. Additional elements (P, S and Al) appearing with Fe minerals along the thaw gradient

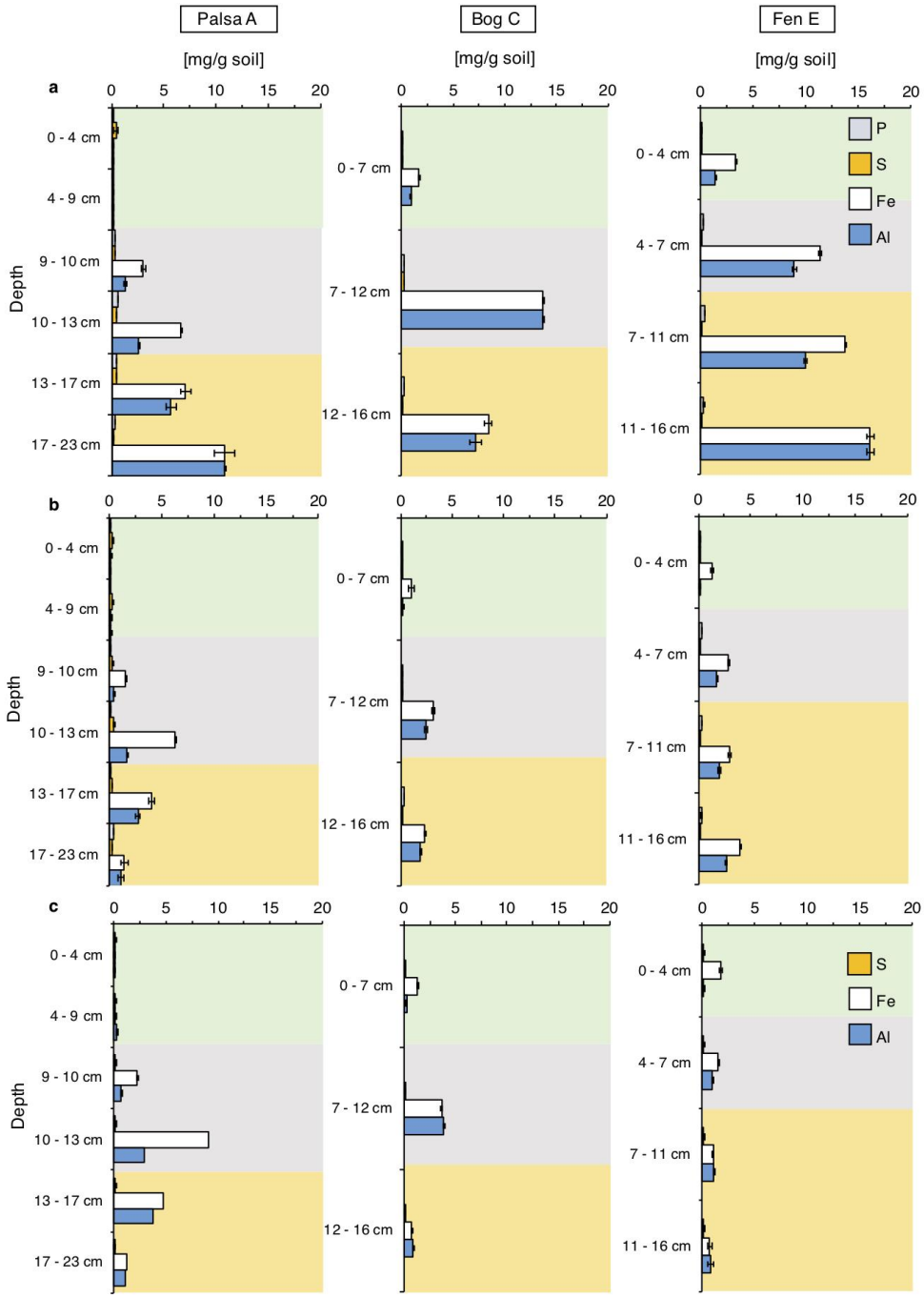

Figure S4. Other elements (P, S, Fe and Al) in extracts of Palsa A, Bog C and Fen E. a, 6M HCl, b, hydroxylamine-HCl and c, sodium pyrophosphate extracted. Phosphorous (P) and sulphur (S) concentrations were measured with ICP-MS, whereas iron (Fe) and aluminum (Al) concentrations were analyzed using MP-AES. The green box marks the organic horizon, grey box the transition zone and yellow box the mineral horizon. Errors indicate the range of duplicate analyses of each layer in ach thaw stage.

S5. Replication along a thaw gradient

To evaluate the consistency of iron and carbon trends along the thaw gradient, 5 cores per thaw stage were analyzed in total. These include:

(1) Palsa A, Bog C and Fen E (discussed in the main text) (1 core per thaw stage)

Cores were taken with a Humax corer and sterile plastic liners in June 2018. This set was immediately split and processed after sampling (3-4 days) (Figure S5, a, yellow cores).

(2) Palsa B, Bog D and Fen F (1 core per thaw stage)

This set was taken at the same time and same conditions as cores Palsa A, Bog C and Fen E, but stored at 4°C for 7 months and then processed (Figure S5, a, white cores).

(3) Triplicate cores in each thaw stage (3 cores per thaw stage)

Triplicate cores in each thaw stage were taken with a Pürckhauer corer in September 2017 and immediately processed after sampling (Figure S5, a, orange, green and blue cores).

All cores showed the same trend for total extractable iron, for the poorly crystalline iron and the total carbon along the thaw gradient. However, we did not directly combine these observations in the main text as there was some variation in the sampling and storage methods.

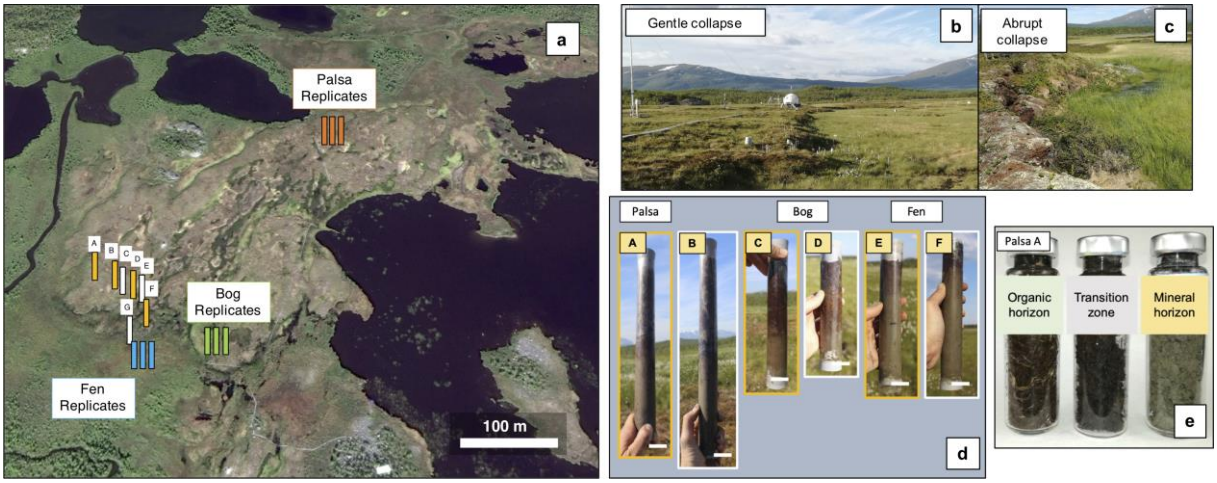

Figure S5. a, Position of cores taken along a thaw gradient at Stordalen mire (Abisko, Sweden). Yellow: Cores were immediately split and processed after sampling (3-4 days). White: Cores were stored at 4°C for 7 months and then processed. The data was compared to triplicate cores in each thaw stage (palsa in orange, bog in green and fen in blue). b, Gentle collapse of palsa sites at Stordalen mire (Abisko, Sweden). The sampled thaw gradient represents a gentle collapse of palsa to bog. c, Abrupt collapse of palsa sites at Stordalen mire (Abisko, Sweden). Permafrost thaw does not necessarily progress through all three thaw stages (palsa, bog and fen). d, Cores taken along a thaw gradient. Palsa: Core A (68°21'18.70"N, 19° 2'38.00"E) and core B (68°21'18.50"N, 19° 2'38.80"E) showed the three main layers in the palsa area: (1) organic horizon, (2) transition zone and (3) mineral horizon. The organic layer was dry and oxic. Bog: Core C (68°21'18.60"N, 19° 2'39.20"E) and core D (68°21'18.30"N, 19° 2'40.00"E) clearly showed the division into the three layers: (1) organic horizon, (2) transition zone and (3) mineral horizon. Both cores were completely water saturated. Fen: Core E (68°21'16.80"N, 19° 2'40.30"E) and core F (68°21'17.80"N, 19° 2'41.30"E) also showed the three layers and were water saturated. The cores represent the active layer in July 2018. The scale bar represents 3 cm. e, Example of the subdivision into (1) organic horizon, (2) transition zone and (3) mineral horizon (Palsa A).

(1) Replicate cores Palsa B, Bog D, Fen F along the thaw gradient

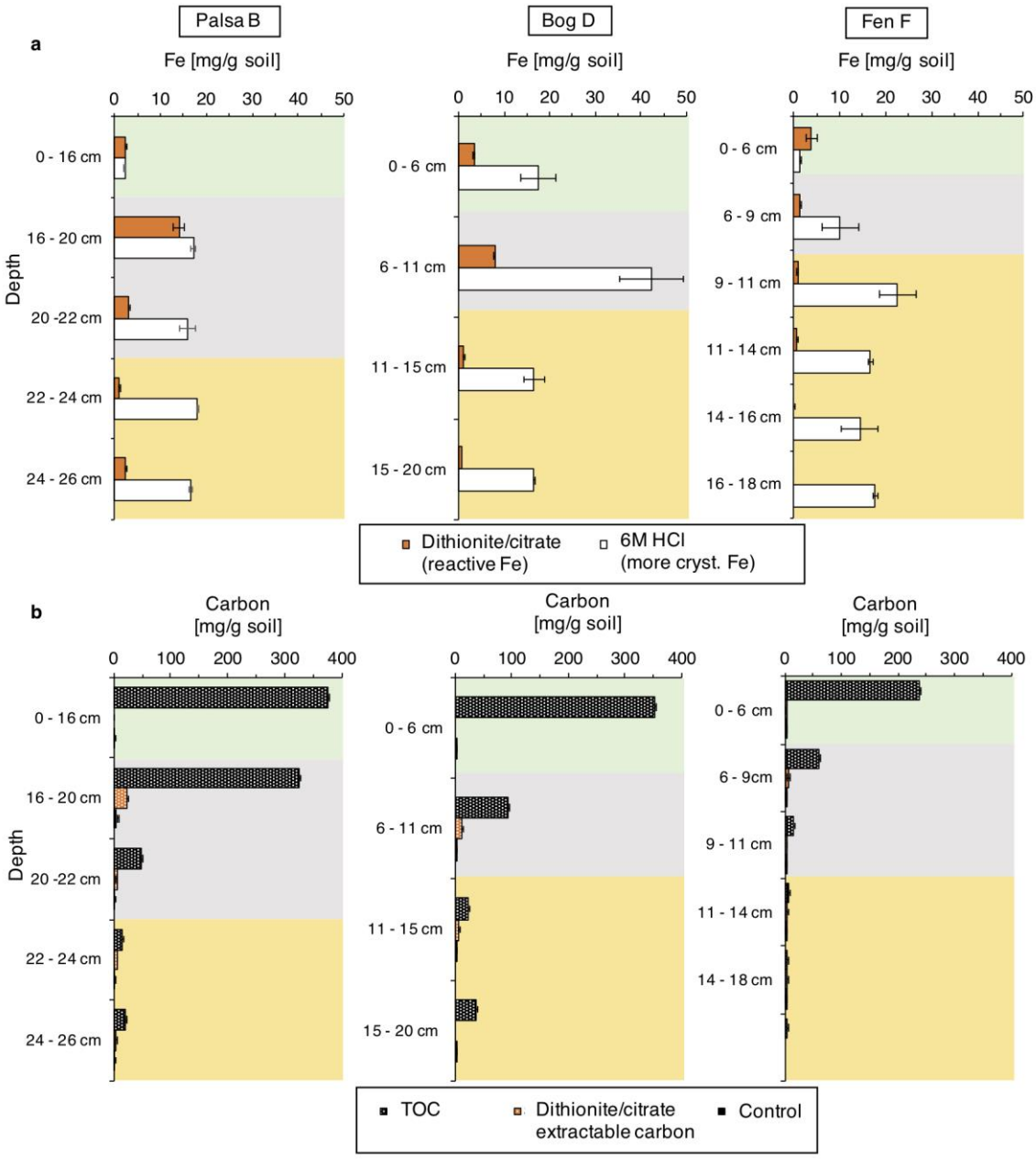

Figure S6. Extractions of replicate cores. a, Iron and b, Carbon concentration of cores Palsa B, Bog D and Fen F. Cores were split after 7 months of incubation at 4°C. The green box marks the organic horizon, grey box the transition zone and yellow box the mineral horizon. Errors indicate the range of duplicate analyses of each layer in each thaw stage. TOC was determined via combustion, whereas the carbon in the dithionite citrate and the control extract (sodium chloride bicarbonate) was determined with the carbon analyzer.

(2) Triplicate cores in each thaw stage (iron analysis)

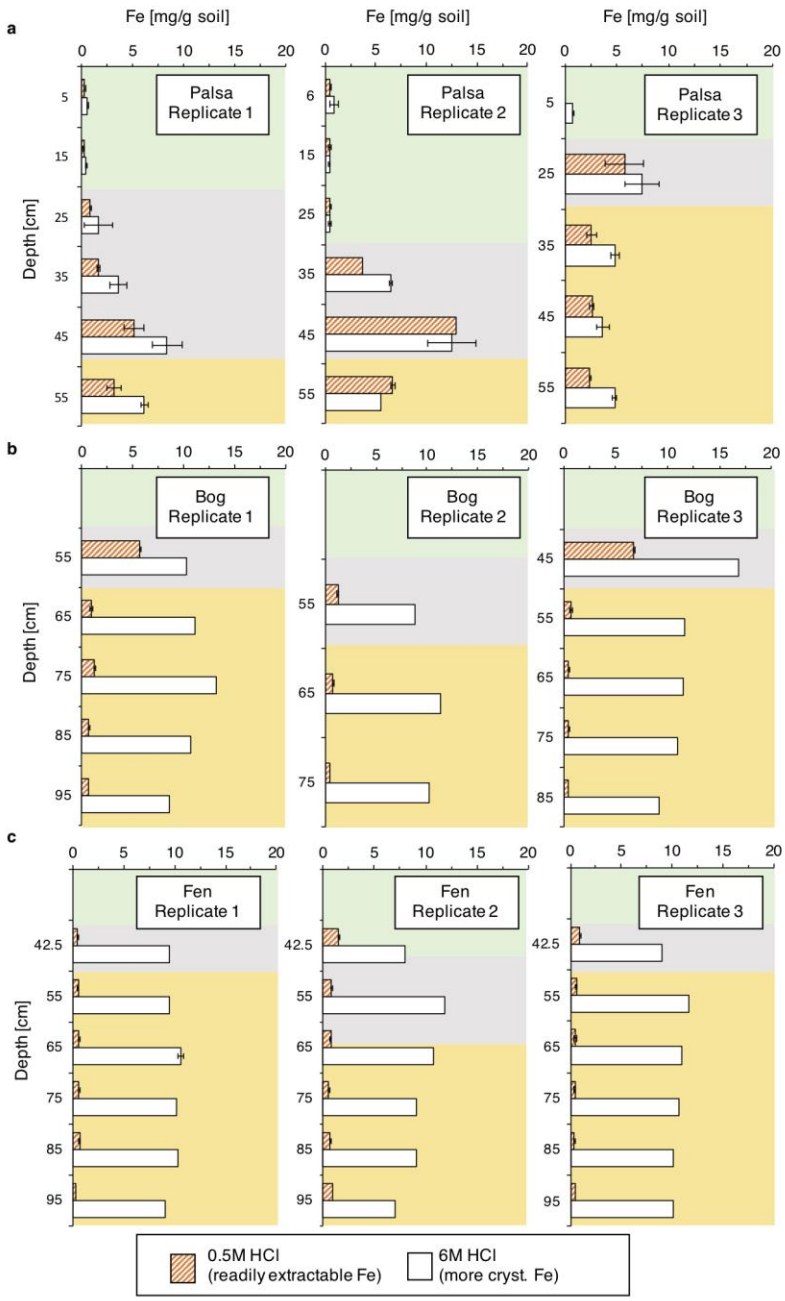

Figure S7. Iron extractions of replicate cores taken with a Pürckhauer corer: a, Palsa (68°21'26.56"N, 19° 3'0.19"E), b, Bog (68°21'16.02"N, 19° 2'49.21"E), c, Fen (68°21'17.16"N, 19° 2'36.29"E). Each core was divided into layers in the field and immediately processed. All replicates represent the active layer in September 2017. The bog and the fen soils were waterlogged. The green box marks the organic horizon, grey box the transition zone and yellow box the mineral horizon. Errors indicate the range of duplicate analyses of each layer in each thaw stage.

(3) Triplicate cores in each thaw stage (carbon analysis)

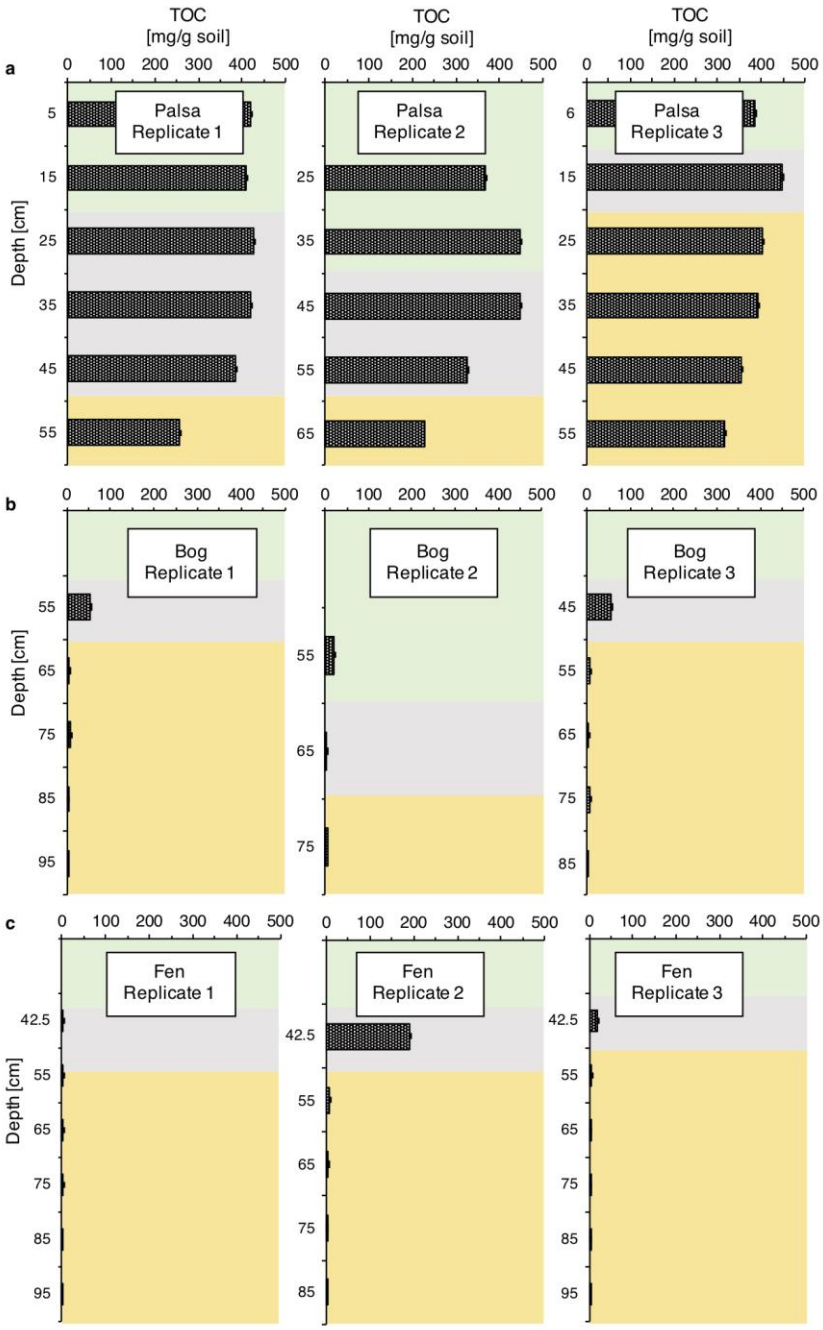

Figure S8. TOC of replicate cores taken with a Pürckhauer corer: a, Palsa (68°21'26.56"N, 19° 3'0.19"E), b, Bog (68°21'16.02"N, 19° 2'49.21"E) and c, Fen (68°21'17.16"N, 19° 2'36.29"E). Each core was divided into layers in the field and immediately processed. All replicates represent the active layer in September 2017. The bog and fen soils were waterlogged. The green box marks the organic horizon, grey box the transition zone and yellow box the mineral horizon. TOC was determined via combustion. Errors indicate the range of duplicate analyses of each layer in each thaw stage.

S6. Replication of nanoSIMS analysis (4 representatives per soil layer)

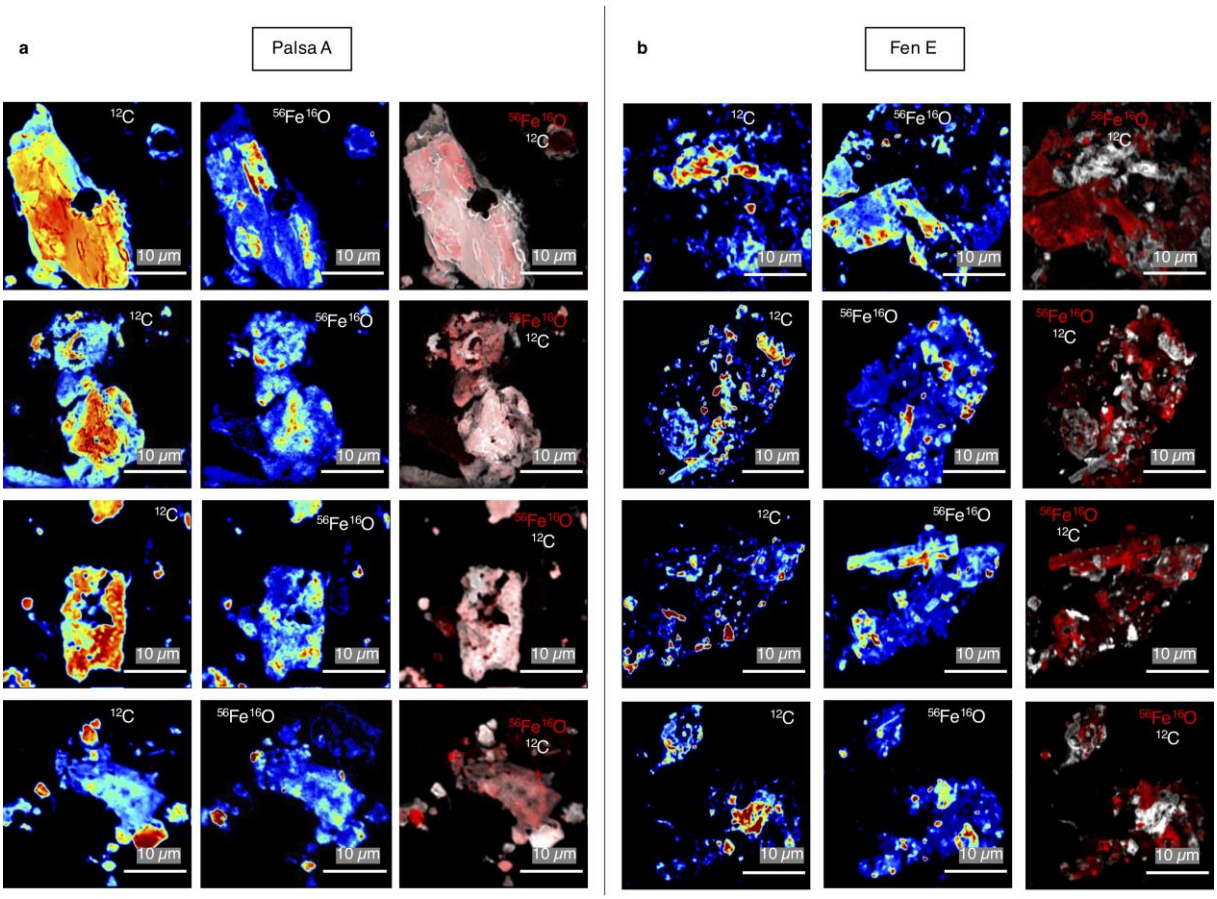

Figure S9. Four representative particles of the fine fraction of a, Palsa A analyzed with nanoSIMS showing a close spatial distribution of Fe and C. Seven detectors were used during nanoSIMS measurements for ^{12}C, $^{56}Fe^{16}O$, ^{16}O, $^{12}C^{14}N$, ^{31}P, ^{32}S and $^{27}Al^{16}O$. ^{12}C and $^{56}Fe^{16}O$ are shown for four representative fine particles plus ^{12}C and $^{56}Fe^{16}O$ distributions, overlain in a single image on the left. Four representative particles of the fine fraction of b, Fen E analyzed with nanoSIMS showing organic-free iron minerals. Seven detectors were used during nanoSIMS measurements for ^{12}C, $^{56}Fe^{16}O$, ^{16}O, $^{12}C^{14}N$, ^{31}P, ^{32}S and $^{27}Al^{16}O$. ^{12}C and $^{56}Fe^{16}O$ are shown for four representative fine particles plus ^{12}C and $^{56}Fe^{16}O$ distributions, overlain in a single image on the left.

S7. Fe(III) reduction by isolated Fe(III)-reducing bacteria from the fen, consuming lactate and forming acetate

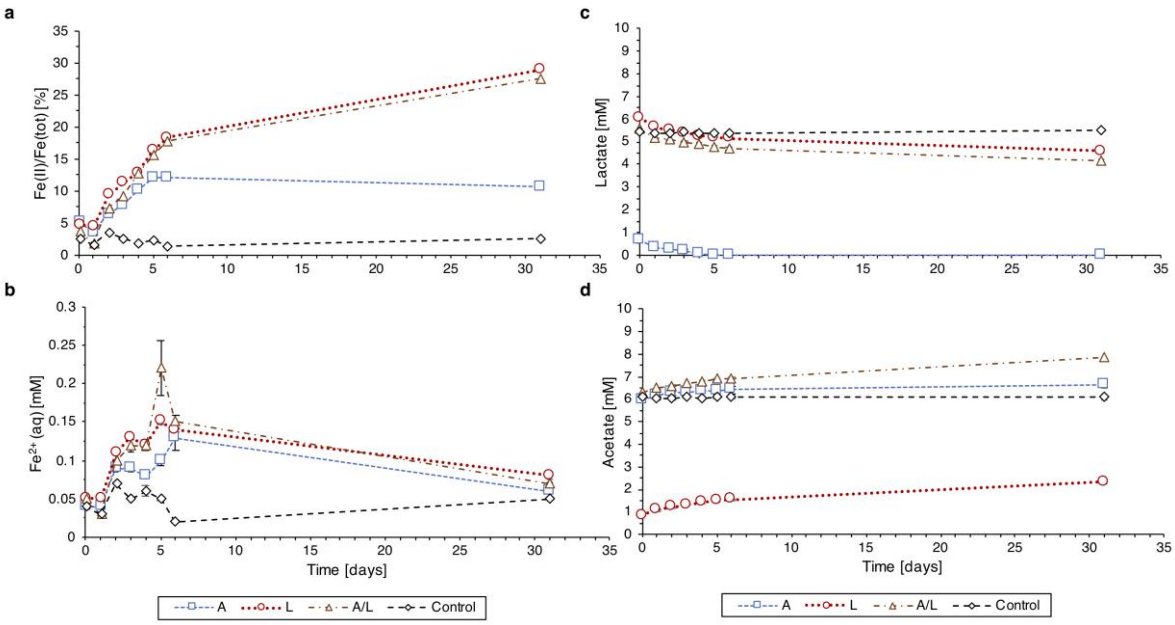

Figure S10. Fe(III) reduction by the Fe(III) reducer isolate from the fen soil core in four experimental setups: only acetate (A), only lactate (L), both acetate and lactate (A/L) and control (no amendments added). a, Fe(II) to Fe(tot) ratio in % in the solid phase over time. 100% would mean that all initial present ferrihydrite was reduced to Fe(II). b, Fe(II) released into the liquid phase over time. c, lactate consumption over time. d, acetate formation over time. Note: The culture which was used for inoculum was previously cultivated in medium supplemented with 5 mM acetate and 5 mM lactate. Therefore, approximately 1 mM of both organic acids were transferred together with the bacteria in all setups, leading to minor Fe(III) reduction also in the acetate only setup using the transferred lactate and forming acetate (0.6 mM) due to residual lactate consumption. After, 31 days, 25% of the initial Fe(III) was reduced to Fe(II) in the solid phase in the lactate only (L) and lactate and acetate (A/L) setup. The lactate concentrations decreased, and the acetate concentration increased by 1.5 mM over 31 days in the lactate amended (L) and (A/L) setup. Some Fe^{2+} was first released into the aqueous phase but later re-adsorbed onto iron minerals, resulting in a decrease in the aqueous Fe^{2+}.